A HIGH SIGNAL-TO-NOISE UV SPECTRUM OF NGC 7469: NEW SUPPORT FOR REPROCESSING OF CONTINUUM RADIATION[1]

Gerard A. Kriss[2,3], Bradley M. Peterson[4], D. Michael Crenshaw[5], and Wei Zheng[3]

To appear in the Astrophysical Journal

ABSTRACT

From 1996 June 10 to 1996 July 29 the International AGN Watch monitored the Seyfert 1 galaxy NGC 7469 using the International Ultraviolet Explorer, the Rossi X-ray Timing Explorer and a network of ground-based observatories. On 1996 June 18, in the midst of this intensive monitoring period, we obtained a high signal-to-noise snapshot of the UV spectrum from 1150–3300 Å using the Faint Object Spectrograph on the Hubble Space Telescope. This spectrum allows us to disentangle the UV continuum more accurately from the broad wings of the emission lines, to identify clean continuum windows free of contaminating emission and absorption, and to deblend line complexes such as Lyα+N V, C IV+He II+O III], Si III]+C III], and Mg II+Fe II. Using the FOS spectrum as a template, we have fit and extracted line and continuum fluxes from the IUE monitoring data. The cleaner continuum extractions confirm the discovery of time delays between the different UV continuum bands by Wanders et al. Our new measurements show delays increasing with wavelength for continuum bands centered at 1485 Å, 1740 Å and 1825 Å relative to 1315 Å with delays of 0.09, 0.28 and 0.36 days, respectively. Like many other Seyfert 1 galaxies, the UV spectrum of NGC 7469 shows intrinsic, blue-shifted absorption in Lyα, N V and C IV. Soft X-ray absorption is also visible in archival ASCA X-ray spectra. The strength of the UV absorption, however, is not compatible with a single-zone model in which the same material absorbs both the UV and X-ray light. Similar to other Seyfert galaxies such as NGC 3516, the UV-absorbing gas in NGC 7469 has a lower ionization parameter and column density than the X-ray absorbing material. While the UV and X-ray absorption does not arise in the same material, the frequent occurrence of both associated UV absorption and X-ray warm absorbers in the same galaxies suggests that the gas supply for each has a common origin.

Subject headings: Galaxies: Active — Galaxies: Individual (NGC 7469) — Galaxies: Seyfert — Ultraviolet: Galaxies — X-Rays: Galaxies

1. INTRODUCTION

For the last year of operations of the International Ultraviolet Explorer (IUE) the International AGN Watch successfully carried out an intensive continuous monitoring campaign on the bright Seyfert 1 galaxy NGC 7469 (Wanders et al. 1997). During the course of these observations we obtained a single high signal-to-noise UV spectrum covering 1150–3300 Å using the Faint Object Spectrograph (FOS) on the Hubble Space Telescope (HST). Simultaneous high-energy X-ray observations were obtained using the Rossi X-ray Timing Explorer (RXTE) (Nandra et al. 1998, and a network of ground-based facilities obtained optical spectra (Collier et al. 1998). These data sets have been used to study the structure of the continuum and line-emitting regions in NGC 7469 using reverberation mapping.

Previous IUE and ground-based campaigns that have applied reverberation mapping techniques to the study of AGN broad-line regions (BLR) have greatly illuminated our understanding of their structure (see the review by Peterson 1993). The reverberation mapping method (Blandford & McKee 1982) uses the light-travel-time delayed response of the emission line clouds to variations in the continuum to unravel the spatial and kinematic structure of the BLR. Campaigns on NGC 5548 and NGC 3783 using IUE (Clavel et al. 1991; Reichert et al. 1994) and again

on NGC 5548 using IUE and HST (Korista et al. 1995) have determined that the BLR is smaller than single-zone photoionization models have suggested, and that it is highly stratified. Inner and outer radii differ by an order of magnitude, and higher ionization lines are characteristically formed in the innermost regions.

Analysis of the IUE data for the NGC 7469 campaign (Wanders et al. 1997) have led to similar results for its broad emission lines. The most remarkable result, however, is the apparent detection of a time delay in the response of different UV continuum windows. The fluxes in bands centered at 1485 Å, 1740 Å, and 1825 Å have cross-correlation centroids with time delays of 0.21, 0.35, and 0.28 days with respect to the flux at 1315 Å. Monte Carlo simulations indicate probable errors of ~ 0.07 days in measuring the delays. Even longer delays ($\sim$1 day) are found for the optical continuum relative to the UV (Collier et al. 1998). A variety of explanations may lead to the observed effects. The most interesting in terms of the overall structure of AGN is that the delays are due to a continuum reprocessing zone near the central continuum source. A more mundane possibility is that the delay is the result of contamination of the flux in the continuum bands by a very broad emission feature such as blended Fe II emission or Balmer continuum emission.

[1] Based on observations with the NASA/ESA *Hubble Space Telescope*, obtained at the Space Telescope Science Institute, which is operated by the Association of Universities for Research in Astronomy, Inc., under NASA contract NAS5-26555. These observations are associated with proposal ID 6747.

[2] Space Telescope Science Institute, 3700 San Martin Drive, Baltimore, MD 21218; gak@stsci.edu

[3] Center for Astrophysical Sciences, Department of Physics and Astronomy, The Johns Hopkins University, Baltimore, MD 21218–2686; zheng@pha.jhu.edu

[4] Department of Astronomy, The Ohio State University, 140 West 18th Avenue, Columbus, OH 43210; peterson@astronomy.ohio-state.edu

[5] Catholic University of America and Laboratory for Astronomy and Solar Physics, NASA Goddard Space Flight Center, Code 681, Greenbelt, MD 20771; crenshaw@buckeye.gsfc.nasa.gov

TABLE 1
FOS OBSERVATIONS OF NGC 7469

Root File Name	Grating	Start Time[a] (UT)	JD (-2450000)	Integration Time (s)
y3b60106t	G130H	19:36:55	252.317	1200
y3b60107t	G130H	20:54:11	252.371	2240
y3b6010at	G190H	22:30:41	252.438	1650
y3b6010bt	G270H	23:06:26	252.463	300

[a] All observations occurred on 1996 June 18.

While this can explain some portion of the UV-continuum delays, as we show later, it is difficult to ascribe the lag of the optical continuum to emission-line contamination.

The higher spectral resolution and higher S/N of the FOS spectrum of NGC 7469 allows a better assessment of the possible contaminants in the chosen IUE continuum intervals. By using the FOS spectrum as a template, a model of the line and continuum emission features can be fitted to the series of IUE spectra. Similar techniques were successfully used on the earlier NGC 3783 (Reichert et al. 1994) and NGC 5548 (Korista et al. 1995) campaigns. This paper describes the FOS data for NGC 7469 and presents new line and continuum flux measurements extracted from the IUE data. In §2 we present the FOS observations and the analysis of that spectrum. In §3 we describe how the template based on the FOS data was fit to the time series of IUE spectra and present a new analysis of the line and continuum variability based on these measurements. In §4 we discuss the UV and X-ray absorbing material in NGC 7469. We discuss our results in §5, and give a summary of our conclusions in §6.

2. FOS OBSERVATIONS

We observed NGC 7469 on 1996 June 18 (UT) using gratings G130H, G190H, and G270H on the blue side of the FOS. These three spectra cover the wavelength range 1150–3300 Å with a resolution of 220 km s^{-1}. The start times and integration times of the observations are given in Table 1. To ensure high S/N, good photometry and accurate flat-fielding, we observed through the 0.86″ aperture and acquired the target using a precision peak-up sequence. The last 5×5 peak up was done using the 0.26″ sec aperture on 0.052″ centers. Centering in the 0.86″ circular aperture was better than 0.04″. The peak flux seen through the 0.26″ aperture at the last peak-up position has a ratio to that seen through the 0.86″ aperture used for the observation consistent with that of a point source. This should alleviate any concern that the spectrum might be contaminated by starlight from a nuclear starburst region.

The standard pipeline calibration applied to the data gives good results. The two G130H observations agree to within 0.5% with each other. A weighted average of these two spectra was taken to produce a mean G130H spectrum. The overlap regions between the G130H, G190H, and G270H spectra agree to better than 1%. In the 14 separate groups read out for the

G130H observation, there is a variation of 3.8% peak to peak. It is smooth and non-random, but could be an instrumental artifact such as thermal variations around the orbit. No renormalizations of the flux scale were applied to any of the spectra.

We used the low ionization Galactic absorption lines to correct the wavelength scale of each observation, assuming that these features are at zero velocity. G130H required a 0.3 Å shift to the blue, as did G270H. The G190H spectrum required no adjustment, but only the Al II λ1670 line is strong enough to measure reliably. We estimate our wavelengths are accurate to ~50 km s^{-1}.

The merged, flux-calibrated spectrum from the four separate observations is shown in Fig. 1. The S/N per pixel (0.25–0.50 Å) is greater than 10 at all wavelengths longward of 1200 Å; per 1 Å it exceeds 20. In addition to the usual broad emission lines and blue continuum, note the pronounced dip in the spectrum at 2200 Å indicative of Galactic extinction, and the broad blends of Fe II emission that become apparent longward of 2000 Å. NGC 7469 also shows high-ionization, intrinsic absorption lines. These are shown in the C IV region in Fig. 2, and they are also present in N V and in Lyα.

To model the lines and continuum in our spectrum, we used the IRAF[1] task specfit (Kriss 1994) to fit a model comprised of a reddened power law in F_λ

$$F_\lambda = F_0 \left(\frac{\lambda}{1000} \right)^{-\alpha},$$

with extinction following the form given by Cardelli, Clayton, & Mathis (1989) with $R_V = 3.1$, multiple Gaussians for the emission lines, single Gaussians for the Galactic and intrinsic absorption lines, and a damped Lorentzian profile for the strong Galactic Lyα absorption. We used the minimum number of Gaussian components necessary to acceptably fit each emission line. For the brightest emission lines, three Gaussians (narrow, broad, and very broad) were typical. An exception is the Si IV+O IV] λ1400 complex. Here we allowed single Gaussians for each line in each multiplet set, with all relative wavelengths linked in proportion to their vacuum values. The widths of the two Si IV lines were linked to be identical, and their flux ratio was fixed at 2:1. The widths of the five O IV] lines were also linked to be identical, but independent of the Si IV lines. Their flux ratios were fixed in the proportion 0.1:0.2:1.0:0.4:0.1 as given by Osterbrock (1963), and the total O IV] flux varied
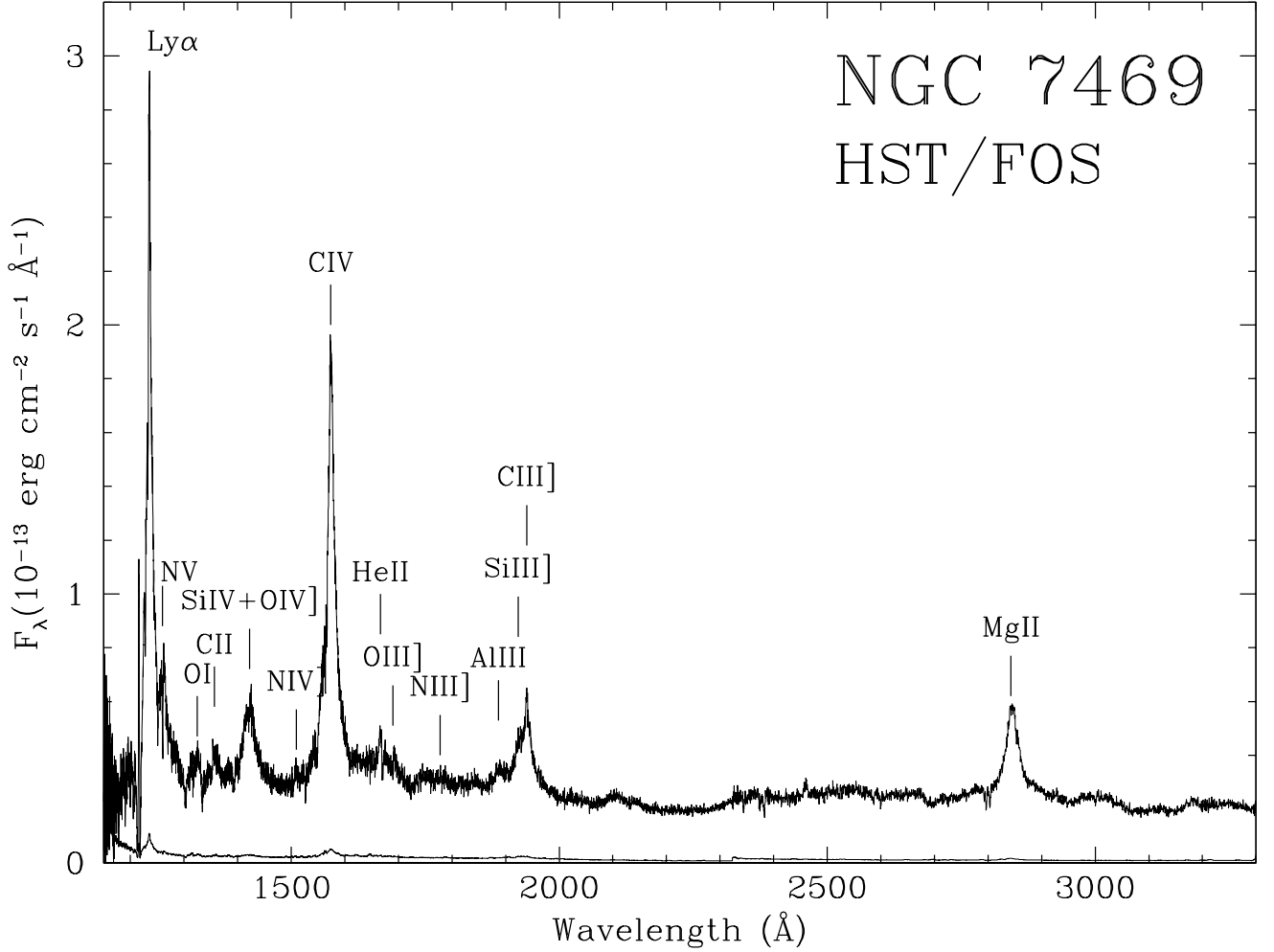
Fig. 1.— Merged, flux-calibrated FOS spectrum of the Seyfert 1 galaxy NGC 7469. The 1-σ statistical errors are the thin line under the data. The most prominent emission lines are labeled.

independently of the Si IV flux.

Our fit covered the wavelength range 1170–3280 Å, excluding an 8 Å window centered on geocoronal Lyα emission. The best-fit χ^2 is 7058 for 5479 points and 183 freely varying parameters. We compute our error bars from the error matrix of the fit assuming a $\Delta\chi^2 = 1$ for a single interesting parameter (Avni 1976).

The best-fit continuum has a normalization of $F_\lambda(1000) = 1.04 \pm 0.01 \times 10^{-13}$ erg cm^{-2} s^{-1} $^{-1}$ and a powerlaw index $\alpha = 0.977 \pm 0.003$. The best fit extinction is $E(B-V) = 0.12 \pm 0.003$, and the column density of the damped Lyα absorption is $3.5 \pm 0.2 \times 10^{20}$ cm^{-2}. (Note that these errors are purely formal, statistical ones. Systematic errors due to our assumption of a continuum shape and due to the exclusion of a large portion of the damped Lyα profile will be larger.) Our measurements are in reasonable agreement with the properties of our own Galaxy along the line of sight. The Elvis, Lockman, & Wilkes (1989) H I survey of AGN sight lines reports an H I column of $4.82 \pm 0.17 \times 10^{20}$ cm^{-2}. Using a gas-to-dust ratio of $N_{HI}/E(B-V) = 5.2 \times 10^{21}$ cm^{-2} (Shull & Van Steenberg 1985) predicts $E(B-V) = 0.09$.
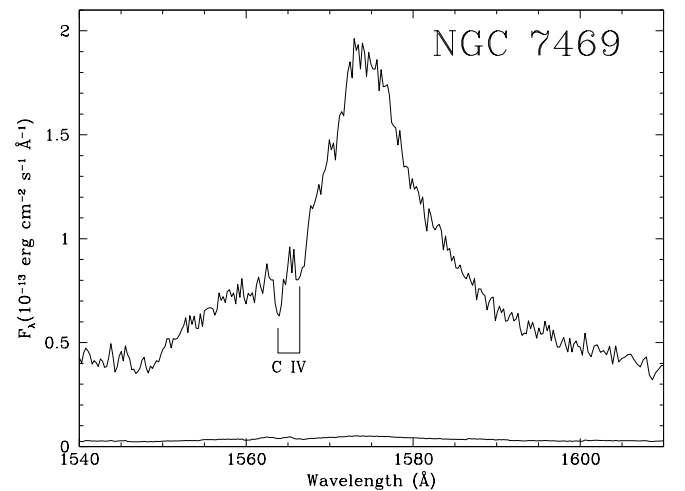

Fig. 2.— The blueshifted intrinsic C IV absorption lines of NGC 7469 are visible in this plot of the C IV emission line region of the spectrum. The 1-σ statistical errors are the thin line under the data.

The individual components for the emission lines are listed in Table 2. Parameters of the blueshifted intrinsic absorption features visible in Lyα, N V, and C IV are given in Table 3. Galactic absorption features are listed in Table 4. The tabulated line widths are not corrected for the instrumental resolution of $220\,\mathrm{km\,s^{-1}}$.

TABLE 2
EMISSION LINE FLUXES IN NGC 7469

Line	λ_{vac} (Å)	Flux[a]	Velocity[b] (km s^{-1})	FWHM (km s^{-1})
Lyα	1215.67	258.0 ± 16.8	-515 ± 21	967 ± 44
Lyα	1215.67	197.0 ± 8.1	-268 ± 33	2932 ± 141
Lyα	1215.67	242.0 ± 19.3	-268 ± 33	10965 ± 560
Lyα total	1215.67	697.0 ± 26.8	$\cdots$	$\cdots$
N V	1240.15	10.4 ± 1.5	389 ± 96	1598 ± 63
N V	1240.15	17.8 ± 2.1	389 ± 96	4949 ± 122
N V	1240.15	48.2 ± 5.7	389 ± 96	12042 ± 575
N V total	1240.15	76.4 ± 2.5	$\cdots$	$\cdots$
Si II	1260.45	6.2 ± 1.0	939 ± 132	2028 ± 346
O I	1304.35	21.0 ± 1.6	-631 ± 169	4618 ± 373
C II	1335.30	21.0 ± 1.4	-165 ± 116	3800 ± 245
Si IV	1393.76	45.2 ± 4.5	-524 ± 62	11665 ± 498
Si IV	1402.77	22.6 ± 2.3	-524 ± 62	11665 ± 498
Si IV total	1396.76	67.8 ± 6.7	$\cdots$	$\cdots$
O IV] total	1402.06	38.0 ± 2.5	-524 ± 62	4002 ± 300
N IV]	1486.50	2.9 ± 0.5	-84 ± 181	1420 ± 307
C IV	1549.05	66.2 ± 4.5	28 ± 14	1598 ± 63
C IV	1549.05	166.0 ± 2.0	-101 ± 23	4949 ± 122
C IV	1549.05	160.0 ± 6.2	-101 ± 23	12042 ± 575
C IV total	1549.05	392.2 ± 7.9	$\cdots$	$\cdots$
Fe II	1608.45	17.7 ± 1.7	-391 ± 190	5498 ± 586
He II	1640.50	4.5 ± 1.6	-81 ± 200	887 ± 443
He II	1640.50	18.5 ± 0.7	-81 ± 200	4949 ± 122
He II	1640.50	32.9 ± 1.2	-81 ± 200	12042 ± 575
He II total	1640.50	55.8 ± 1.8	$\cdots$	$\cdots$
O III]	1663.48	2.5 ± 0.2	391 ± 97	790 ± 210
N III]	1750.51	27.2 ± 2.8	-210 ± 399	8222 ± 719
Al III	1857.40	18.5 ± 1.6	412 ± 157	4461 ± 553
Si III]	1892.03	19.1 ± 3.9	-7 ± 138	2470 ± 160
C III]	1908.73	4.3 ± 0.9	-77 ± 29	547 ± 99
C III]	1908.73	42.9 ± 4.9	142 ± 136	3160 ± 204
C III]	1908.73	75.0 ± 4.1	142 ± 136	17050 ± 1264
C III] total	1908.73	122.2 ± 6.5	$\cdots$	$\cdots$
Mg II	2798.74	9.2 ± 1.8	56 ± 15	1195 ± 136
Mg II	2798.74	90.0 ± 1.8	56 ± 15	3426 ± 72
Mg II	2798.74	59.5 ± 2.9	56 ± 15	21393 ± 662
Mg II total	2798.74	158.7 ± 3.9	$\cdots$	$\cdots$

[a]Observed flux in units of $10^{-14}\,\mathrm{erg\,cm^{-2}\,s^{-1}}$.
[b]Velocity is relative to a systemic redshift of $cz = 4916\,\mathrm{km\,s^{-1}}$ (de Vaucouleurs et al. 1991).

TABLE 3
INTRINSIC ABSORPTION LINES IN NGC 7469

Line	λ_{vac} (Å)	EW (Å)	Velocity (km s^{-1})	FWHM (km s^{-1})
Lyα	1215.67	0.41 ± 0.08	-1870 ± 17	280 ± 58
Lyα	1215.67	5.04 ± 0.30	-656 ± 24	1439 ± 61
N V	1238.82	0.48 ± 0.08	-1834 ± 20	309 ± 57
N V	1242.80	0.24 ± 0.07	-1834 ± 20	309 ± 57
C IV	1548.19	0.45 ± 0.05	-1819 ± 11	275 ± 27
C IV	1550.77	0.35 ± 0.04	-1819 ± 11	275 ± 27

[a]Velocity is relative to a systemic redshift of $cz = 4916\,\mathrm{km\,s^{-1}}$ (de Vaucouleurs et al. 1991).

3. IUE SPECTRA

3.1. *Measuring Continuum and Emission-line Fluxes*

Analysis of the IUE spectra of NGC 7469 during the summer 1996 monitoring campaign (Wanders et al. 1997) suggests a time delay in the responses of the longer wavelength UV continuum bands relative to the shortest wavelength bin centered at 1315 Å. One possible explanation for these delays is that the

IUE measurements are not using pure continuum, and that light from broadly distributed line emission in the spectrum might be contaminating the data. Our fits to the FOS data allow us to examine the degree of contamination. Fig. 3 shows the FOS spectrum of NGC 7469 scaled to provide a good view of the continuum. The bands used for the IUE measurements are indicated, and the best-fit reddened powerlaw is also shown. Note that only in the 1485 Å band does the fitted continuum pass through the actual data points.
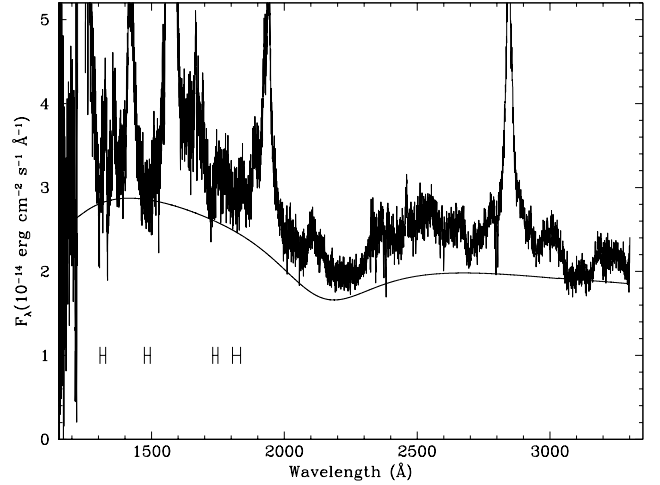

FIG. 3.— The best fit powerlaw continuum for the NGC 7469 is shown as the thin solid line. The dip at 2200 Å and the downturn at the short wavelength end reflect the extinction of $E(B-V) = 0.12$. At most points in the spectrum, the blended wings of the broad emission lines and Fe II emission contribute a substantial amount of overlying flux. The four "continuum" windows used for measuring the fluxes in the IUE spectra are shown as heavy solid bars.

TABLE 4
GALACTIC ABSORPTION LINES IN NGC 7469

Line	λ_{vac} (Å)	EW (Å)	Velocity (km s^{-1})	FWHM (km s^{-1})
Si II	1190.42	0.16 ± 0.11	20 ± 54	211 ± 150
Si II	1193.14	0.12 ± 0.14	80 ± 93	211 ± 150
N I	1200.16	0.39 ± 0.17	-117 ± 60	303 ± 119
Si III	1206.50	1.07 ± 0.22	-186 ± 45	593 ± 112
S II	1250.58	0.23 ± 0.07	-141 ± 0	303 ± 41
S II	1253.00	0.21 ± 0.06	60 ± 53	303 ± 41
S II	1259.52	0.26 ± 0.07	-26 ± 50	303 ± 41
Si II	1260.42	0.58 ± 0.09	7 ± 20	303 ± 41
O I	1302.17	0.41 ± 0.07	-2 ± 28	303 ± 41
Si II	1304.37	0.36 ± 0.07	-60 ± 31	303 ± 41
C II	1334.53	0.32 ± 0.16	-290 ± 47	433 ± 112
C II	1335.69	0.68 ± 0.19	-290 ± 47	433 ± 112
Si IV	1393.76	0.97 ± 0.16	-97 ± 58	950 ± 140
Si IV	1402.77	0.62 ± 0.15	-68 ± 91	950 ± 140
Si II	1527.17	0.45 ± 0.06	-55 ± 21	314 ± 91
C IV	1548.19	0.38 ± 0.07	-325 ± 44	390 ± 57
C IV	1550.77	0.43 ± 0.07	-325 ± 44	390 ± 57
Fe II	1608.45	0.27 ± 0.07	62 ± 45	314 ± 91
Al II	1670.79	0.52 ± 0.31	-57 ± 17	314 ± 91
Fe II	2344.21	0.32 ± 0.10	-3 ± 89	518 ± 58
Fe II	2374.46	1.05 ± 0.16	20 ± 39	518 ± 58
Fe II	2382.77	1.11 ± 0.18	-113 ± 36	518 ± 58
Fe II	2586.65	0.78 ± 0.11	-104 ± 44	518 ± 58
Fe II	2600.17	0.60 ± 0.10	-48 ± 46	518 ± 58
Mg II	2796.35	0.57 ± 0.07	-1 ± 11	230 ± 27

Fig. 4 illustrates the degree of contamination in more detail with magnified views of each of the continuum bands along with the fitted continuum. The shortest wavelength bin centered on 1315 Å is contaminated by O I $\lambda 1304$ emission. Only
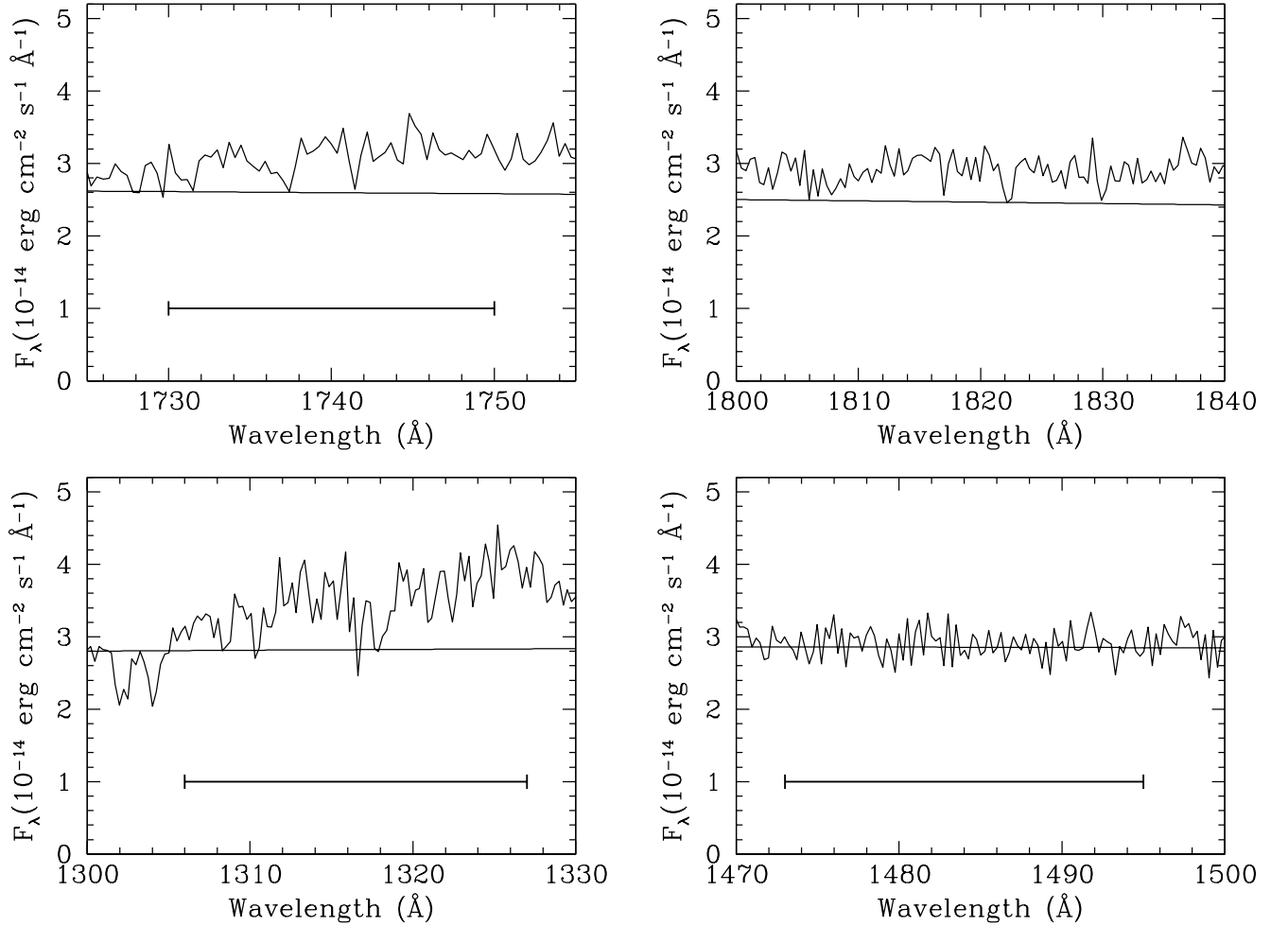
FIG. 4.— The four panels give a close up view of the continuum windows used for the IUE flux measurements. The heavy solid bars show the wavelength intervals used. Upper left: $F_\lambda(1740\text{Å})$; upper right: $F_\lambda(1825\text{Å})$; lower left: $F_\lambda(1315\text{Å})$; lower right: $F_\lambda(1485\text{Å})$. O I $\lambda1304$ emission contaminates the $F_\lambda(1315\text{Å})$ window, and blended Fe II emission contaminates the $F_\lambda(1740\text{Å})$ and the $F_\lambda(1825\text{Å})$ windows. Only the $F_\lambda(1485\text{Å})$ is pure continuum.

78% of the flux in the IUE measurement bin is from the fitted continuum. The two longest wavelengths bins, 1740 Å and 1825 Å, are each contaminated by Fe II emission. Within the IUE measurement bins the percentage of flux due to the fitted continuum is 81% and 85%, respectively. The bin at 1485 Å is relatively clean. 99% of the flux in the IUE measurement bin is due to the fitted continuum.

Our new analysis of the IUE spectra from the 1996 campaign aims to obtain clean measurements of the continuum and deblended measurements of the emission lines using the FOS spectrum as a template. For the fits described below we used only the TOMSIPS-extracted spectra described by Wanders et al. (1997). As noted by Wanders et al., these spectra appear slightly smoother to the eye and have slightly smaller error bars. In the initial analysis by Wanders et al., both the TOMSIPS and NEWSIPS data gave similar results. Table 1 of Wanders et al. (1997) logs 219 spectra obtained using IUE. We have restricted our analysis to the 207 spectra unaffected by target centering problems or short exposure times, i.e., we have eliminated all spectra with notes 1–4 from Table 1 of Wanders et al. The mean of these spectra is shown as Figure 1 of Wanders et al.

Using the model fit to the FOS data in §2, we developed a template for fitting the series of IUE spectra by first fitting the

mean IUE spectrum. The best-fit continuum has a normalization of $F_\lambda(1000) = 1.37 \times 10^{-13}$ erg cm^{-2} s^{-1} $^{-1}$ and a powerlaw index $\alpha = 0.913 \pm 0.003$, close to the shape and intensity of the FOS snapshot. Emission-line fluxes, wavelengths, and widths are listed in Table 5, and absorption-line parameters are given in Table 6. The resulting best-fit model is shown overlayed on the mean IUE spectrum in Fig. 5; the residuals shown in the lower panel have an rms of a few percent of the spectral intensity.

Due to the lower resolution and lower S/N of the individual IUE spectra, numerous constraints were imposed on the use of this template for the fits to the individual spectra. For example, the wavelengths of weak emission lines were tied to that of C IV $\lambda1549$ by the ratios of their laboratory values; the widths of weak lines were fixed at the values obtained in a fit to the mean IUE spectrum; the wavelengths of multiple components of strong lines were all fixed at the same wavelength; the parameters of all absorption features were fixed at the values obtained in the fit to the mean IUE spectrum. This left 44 free parameters for the fit to each spectrum: the power-law normalization and exponent; the fluxes of the individual emission lines; and the wavelengths and widths of the bright emission lines. Each spectrum was then fit using `specfit`. To provide initial parameters for each fit, we used the best fit to the mean spectrum as a

starting point. The continuum normalization was then scaled by the ratio of the 1485 Å continuum flux to the same continuum flux in the mean spectrum; line fluxes were scaled by the ratio of the integrated net C IV flux to the same flux measured in the mean spectrum; line wavelengths were shifted by the location of the peak of the C IV line relative to its location in the mean spectrum.

TABLE 5
EMISSION LINE FLUXES IN THE MEAN
IUE SPECTRUM OF NGC 7469

Line	λ_{vac} (Å)	Flux[a]	Velocity[b] (km s^{-1})	FWHM (km s^{-1})
Lyα	1215.67	86.4	−622	1122
Lyα	1215.67	156.0	−622	2144
Lyα	1215.67	150.0	−622	8134
Lyα total	1215.67	392.4	⋯	⋯
N V	1240.15	25.9	−513	2405
N V	1240.15	22.7	−513	6292
N V	1240.15	61.3	−513	14764
N V total	1240.15	109.9	⋯	⋯
Si II	1260.45	3.0	747	3000
O I	1304.35	13.6	−823	4700
C II	1335.30	13.8	−322	3850
Si IV	1393.76	39.9	−881	11521
Si IV	1402.77	20.0	−871	11521
Si IV total	1396.76	59.9	⋯	⋯
O IV]	1402.06	20.8	−303	3510
N IV]	1486.50	1.1	−384	1000
C IV	1549.05	79.0	−103	2405
C IV	1549.05	137.0	−103	6292
C IV	1549.05	126.0	−103	14764
C IV total	1549.05	342.0	⋯	⋯
He II	1640.50	8.0	−153	1716
He II	1640.50	22.0	−153	6292
He II	1640.50	39.2	−153	14764
He II total	1640.50	69.2	⋯	⋯
O III]	1663.48	0.5	412	1795
N III]	1750.51	22.4	−783	7821
Al III	1857.40	9.4	−192	4387
Si III]	1892.03	14.4	−635	2557
C III]	1908.73	3.0	−460	1063
C III]	1908.73	35.2	−460	3143
C III]	1908.73	57.7	−460	17552
C III] total	1908.73	95.9	⋯	⋯

[a]Observed flux in units of 10^{-14} erg cm^{-2} s^{-1}.
[b] Velocity is relative to a systemic redshift of $cz = 4916$ km s^{-1} (de Vaucouleurs et al. 1991).

Using the best-fit parameter values for each spectrum, we derived fluxes for the quantities of interest. Initial error bars were assigned based on the statistical 1-σ values obtained from specfit. Final error bars were calculated using a procedure common to our previous work in International AGN Watch campaigns. We conservatively assume that there is no variation in flux between two data points with a time separation < 0.25 d. (The mean separation between observations is 0.23 d.) We then scale the initial error bars so that their mean fractional uncertainty is equal to the root-mean-square (rms) of the distribution of flux ratios for all data pairs in the time series with $\Delta t < 0.25$ d (Rodríguez-Pascual et al. 1997; Wanders et al. 1997). Note that the resulting error bars are an upper limit if there is any residual intrinsic variability on timescales shorter than successive observations in the time series. The derived fluxes and errors are shown as light curves described in the next section. The actual data points and error bars can be ob-

tained from the International AGN Watch web site at the URL http://www.astronomy.ohio-state.edu/~agnwatch/#da

TABLE 6
ABSORPTION LINES IN THE MEAN
IUE SPECTRUM OF NGC 7469

Line	λ_{vac} (Å)	EW (Å)	Velocity (km s^{-1})	FWHM (km s^{-1})
Lyα	1215.67	0.39	−1898[a]	1500
Lyα	1215.67	5.06	−661[a]	2000
N V	1238.82	1.17	−2215[a]	1455
N V	1242.80	1.72	−1595[a]	1455
C IV	1548.19	0.46	−1851[a]	990
C IV	1550.77	0.36	−1841[a]	990
S II	1250.58	0.18	−141[b]	1455
S II	1253.00	0.20	36[b]	1455
S II	1259.52	0.25	−33[b]	1380
Si II	1260.42	0.56	2[b]	1380
O I	1302.17	0.47	−840[b]	1255
Si II	1304.37	0.47	−899[b]	1255
C II	1334.53	0.25	−892[b]	1170
C II	1335.69	0.50	−884[b]	1170
Si IV	1393.76	0.51	−391[b]	1638
Si IV	1402.77	0.32	−391[b]	1638
Si II	1527.17	0.41	−585[b]	990
C IV	1548.19	0.34	−380[b]	990
C IV	1550.77	0.54	−369[b]	990
Fe II	1608.45	0.23	58[b]	995
Al II	1670.79	0.39	−20[b]	1000

[a]Intrinsic absorption feature. Velocity is relative to a systemic redshift of $cz = 4916$ km s^{-1} (de Vaucouleurs et al. 1991).
[b]Galactic feature. Velocity is heliocentric.

We note that our use of a global power-law model for the underlying continuum means that not all the continuum flux measurements we tabulate are statistically independent. The power-law model contains only two free parameters, its normalization and the spectral index. Thus in effect only two of the continuum fluxes suffice to describe the data set at a single point in time.

3.2. *Continuum and Emission-line Light Curves*

The newly derived continuum light curves are shown in Fig. 6. These are quite similar to the original data presented in Wanders et al. All curves show the 10–15 day "events" superposed on a gradual decrease in flux from the start to the end of the campaign. There are subtle differences, however, that are only apparent in a ratio between the new measurements and the originals. Light curves of these ratios are shown in Fig. 7. All four light curves show slight differences from the originals throughout the "event" centered on day 280. The most apparent differences are in the light curve for F(1825 Å), which shows departures from the original surrounding all peaks in the light curve. The sense of the difference is that when the source is brighter, more of the 1825 Å flux is due to continuum light.

The emission-line light curves are also quite similar to those of Wanders et al. These are shown in Figures 8–10. Note that our deblending process has recovered more signal in the N V and the He II light curves. None of the weaker lines, however, show any strong correlation with the events in the continuum light curves.
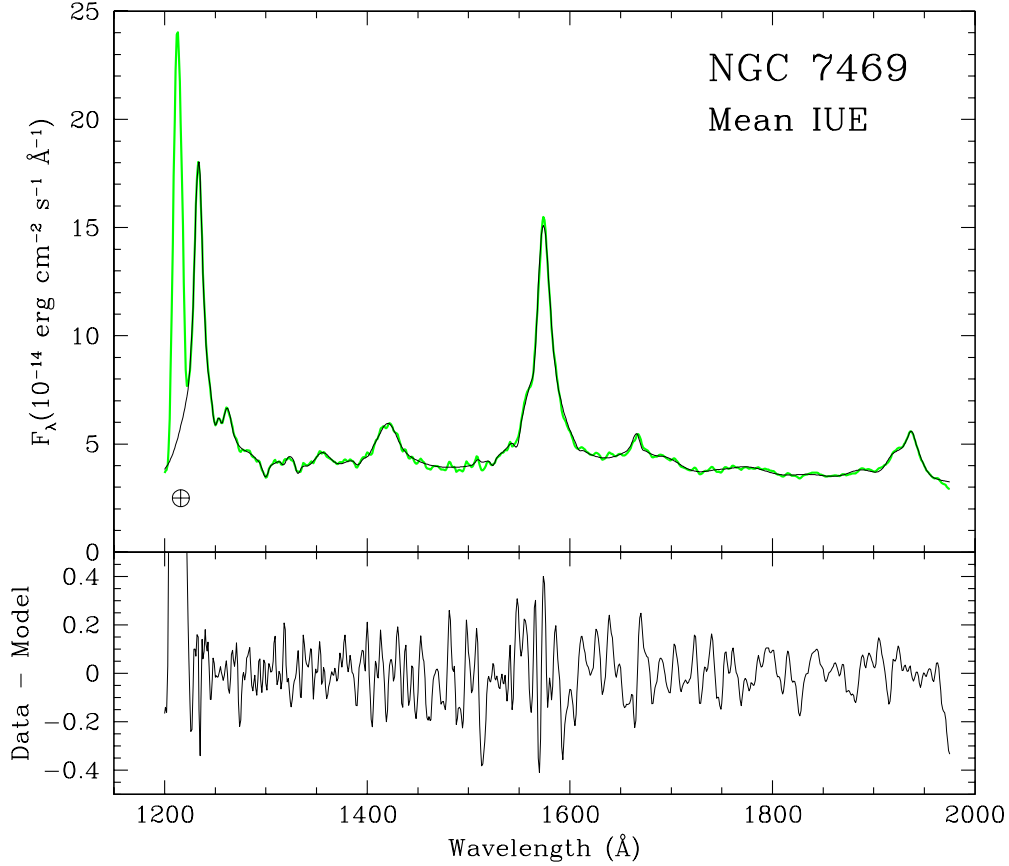
Fig. 5.— Mean IUE spectrum of the Seyfert 1 galaxy NGC 7469 (gray curve) overlayed with the best-fit model based on the FOS spectrum (thin black curve). Geocoronal Lyα emission is indicated by ⊕. The lower panel shows the residuals to the fit.

3.3. Variability Characteristics

To quantify the characteristics of the variability in our new measurements, we use the standard parameters adopted by the International AGN Watch. We summarize these for all our measured fluxes in Table 7. The mean flux, $\overline{F}$, and the sample standard deviation (or root-mean-square flux), σ_F, have their usual statistical definitions. The third parameter, F_{var}, is the fractional variation in the flux corrected for measurement errors:

$$F_{var} = \frac{\sqrt{(\sigma_F^2 - \Delta^2)}}{\overline{F}}, \qquad (1)$$

where Δ^2 is the mean square value of the individual measurement errors. The fourth parameter, R_{max}, is the ratio of the maximum flux to the minimum flux. Note that both of these latter quantities are not very useful for weaker line fluxes where the measurement uncertainty is much larger than any intrinsic variations.

For the continuum measurements listed in Table 7, our fitted fluxes show fractional variations and ratios of maximum to minimum flux that are slightly greater than or equal to that seen in the original data, showing that we have probably eliminated some small amount of less-variable contamination in our fitting process. In contrast, the fractional variability in the strong emission lines has either stayed the same or decreased. This is likely due to the broad wings we have included in our line flux measurements. As one can see in the rms spectrum shown in

TABLE 7
VARIABILITY PARAMETERS

Feature	N_{data}	$\overline{F}$[a]	σ_F^{a}	F_{var}	R_{max}^{b}
F_λ(1315 Å)	207	3.80	0.62	0.16	2.15
F_λ(1485 Å)	207	3.85	0.56	0.14	1.95
F_λ(1740 Å)	207	3.52	0.45	0.12	1.82
F_λ(1825 Å)	207	3.34	0.41	0.11	1.83
Lyα	207	396.77	57.09	0.12	2.13
Lyα+N V	207	504.18	65.50	0.12	1.95
N V	207	107.42	32.33	0.23	(7.83)
Si IV	207	82.96	22.12	0.21	4.45
C IV	207	343.10	34.44	0.07	1.80
He II	207	69.33	19.42	0.20	(7.19)
C III]	207	110.42	42.51	0.22	(6.36)
Si II	207	3.38	2.84	0.62	(857)
O I	207	13.00	4.27	0.27	(10.9)
C II	207	13.17	4.26	0.24	(52.4)
N IV]	207	1.54	1.50	0.68	(467)
O III]	207	10.87	4.68	0.36	(23.0)
N III]	207	22.64	8.77	0.29	(21.7)
Si III]	207	14.01	4.73	0.23	(13.8)
Si III]+C III]	207	124.43	42.04	0.19	(4.74)

[a]Units are 10^{-14} ergs cm^{-2} s^{-1} Å^{-1} for continuum fluxes and 10^{-14} ergs cm^{-2} s^{-1} for line fluxes.
[b]Uncertain values enclosed in parentheses are dominated by noise.

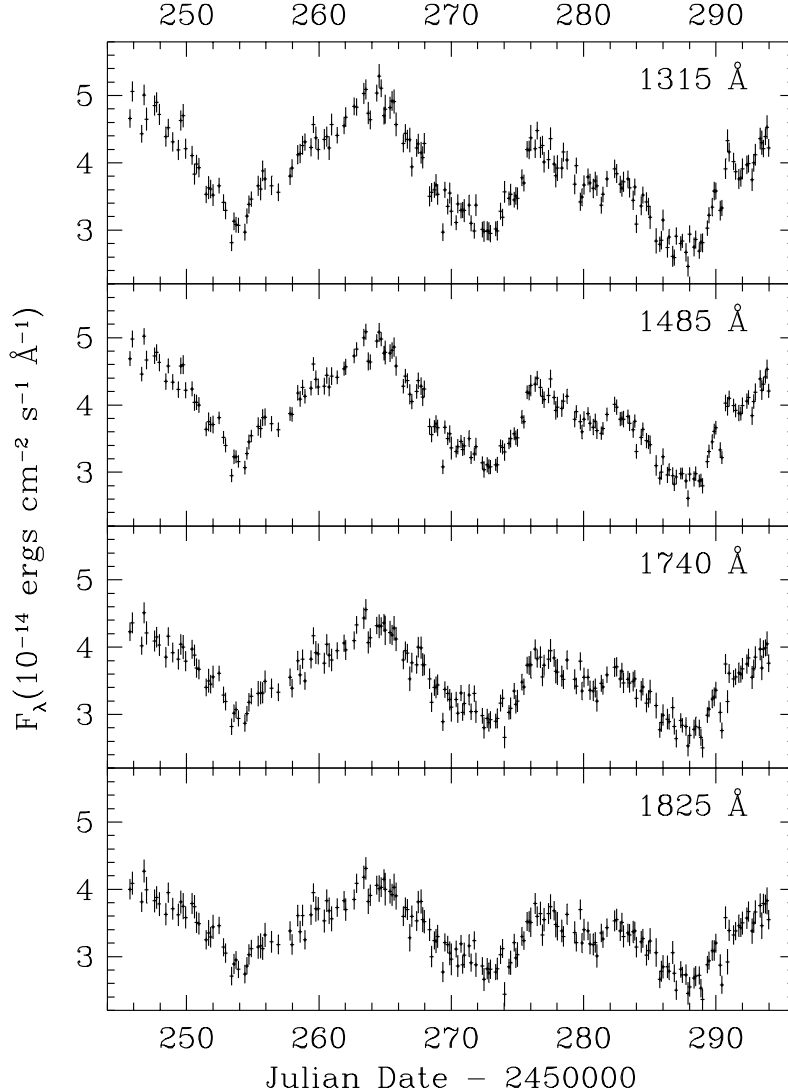Figure 1 of Wanders et al., the most variable portion of each

FIG. 6.— Light curves for the continuum fluxes from the 1996 campaign on NGC 7469 extracted from the IUE spectra using the FOS spectrum as a template.

emission line is the line core. The contrast of this core is less in the fits we have done using the FOS spectral template.

3.4. *Cross-correlation Analysis*

To re-examine the question of whether there are genuine time delays between the continuum variations at different wavelengths, we have performed a cross-correlation analysis of our newly extracted fluxes. We have used both the interpolation cross-correlation function (ICCF) (Gaskell & Sparke 1986; Gaskell & Peterson 1987), and the discrete cross-correlation function (DCF) (Edelson & Krolik 1988). Both algorithms use code as implemented by White & Peterson (1994). We show the derived cross-correlation functions for the continuum fluxes and bright emission lines in Fig. 11; the CCFs for the weak emission lines are shown in Fig. 12.

We have made several measurements to quantify the characteristics of the cross-correlation functions for each measured feature. In Table 8 we list the time delay for the centroid of the peak in the CCF, τ_{cent}, the time delay at which the peak occurs, τ_{peak}, the peak amplitude, r_{max}, of each CCF and the full-width at half-maximum (FWHM) of the peak. We calculate the cen-troids using only CCF values exceeding 80% of the peak amplitude. As the results measured from both the ICCF and DCF curves are nearly identical, the tabulated numbers are based on the ICCF results. The error bars for τ_{cent} and τ_{peak} are based on model-independent Monte Carlo simulations using randomized fluxes and a random subset selection method as described by Peterson et al. (1998). Random noise contributions are added to each flux measurement in a light curve, and a random subset of data pairs is selected for analysis. This process is repeated many times in a procedure analogous to "bootstrapping". Analysis of the resulting distributions from the simulations leads to the error bars quoted in Table 8 for τ_{cent} and τ_{peak}. We note that the smallest of these errors are a factor of ~ 2 smaller than the average sampling interval of ~ 0.2 days, and they are only valid if there is little variability on timescales shorter than this interval. High-time-resolution observations of NGC 7469 obtained by Welsh et al. (1998) show that this assumption is valid.

Compared to the results of Wanders et al., the amplitudes of the continuum CCFs are generally slightly higher, the amplitudes of the emission-line CCFs are generally lower, and the
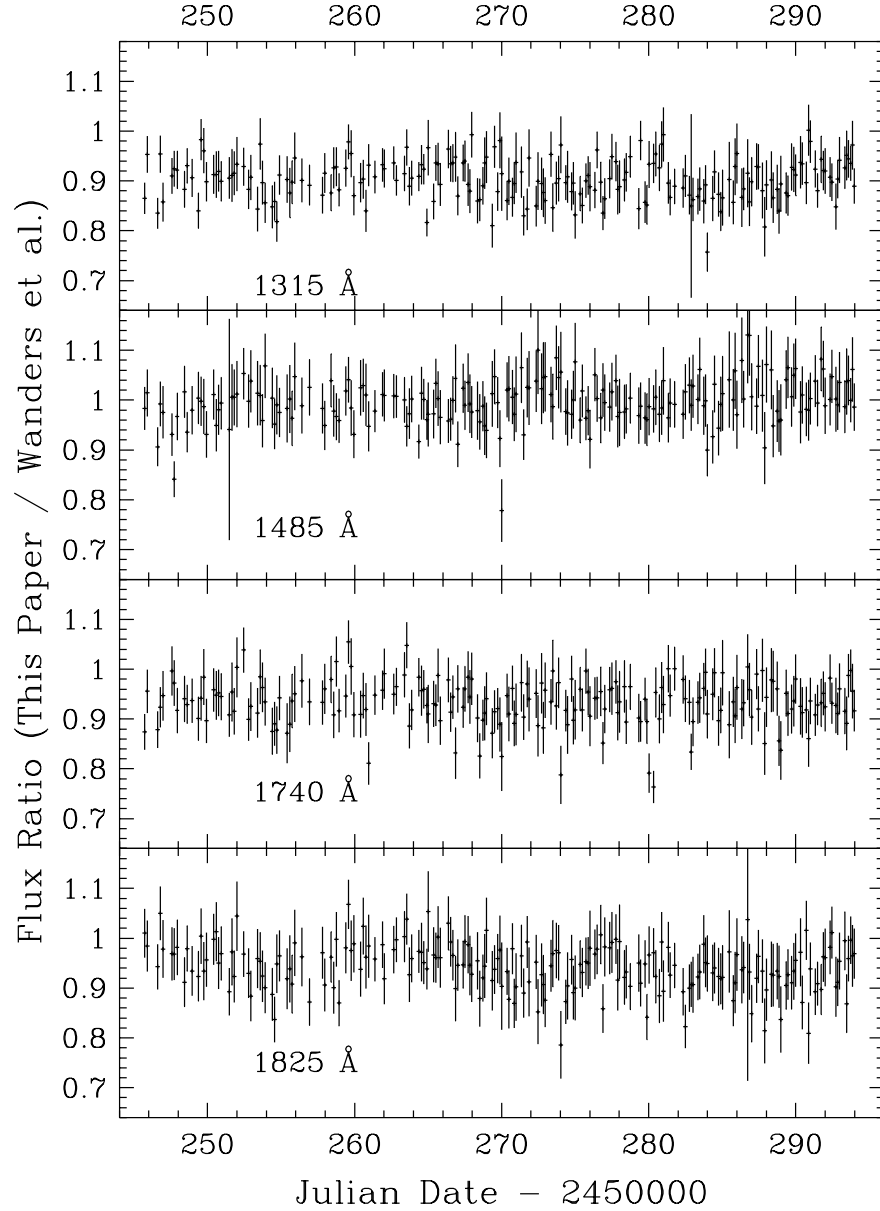
FIG. 7.— Light curves of the ratios of the newly measured continuum fluxes shown in Figure 6 to the original continuum fluxes from Wanders et al. (1997).

time delays measured from our CCFs are a bit shorter. The difference in amplitudes reflects our previous results on the difference in variability amplitudes— the continuum measurements are indeed cleaner, free of low-variability contaminants, and the emission-line measurements have a greater contribution from the low-variability broad wings.

The apparently cleaner continuum measurements now permit a critical re-examination of the question of time delay as a function of wavelength. Our measured time delays differ from those of Wanders et al., *but the lag at long wavelengths relative to short wavelengths is still there, at roughly the same level.* Relative to the flux at 1315 Å, the fluxes at 1485 Å, 1740 Å and 1825 Å have time delays of 0.09, 0.28, and 0.36 days, respectively, compared to the values of 0.19–0.22, 0.32–0.38 and 0.22–0.35 days found by Wanders et al.

As noted in §3.2, effectively only two of the four continuum flux measurements are statistically independent due to the

global power-law fit we have used to describe the continuum. Therefore, although Table 8 shows a monotonically increasing time delay with wavelength, the monotonic nature is largely a consequence of the global constraints we have imposed on the continuum shape. To assess the influence such a global constraint imposes on our measured cross-correlation functions, we have performed another Monte Carlo experiment using the time series of the measured power-law normalizations and spectral indices. Starting with the power-law fit parameters builds in the global linkages between the four wavelength intervals. As in the random subset selection method described by Peterson et al. (1998), we chose a random subset from the series of flux normalization points and indices, preserving the time order of the points. At the selected time points in a given subset, the normalizations and indices were assigned random values from a Gaussian distribution with a mean of the measured value at that time and a dispersion of the 1σ error bar. From these simu-
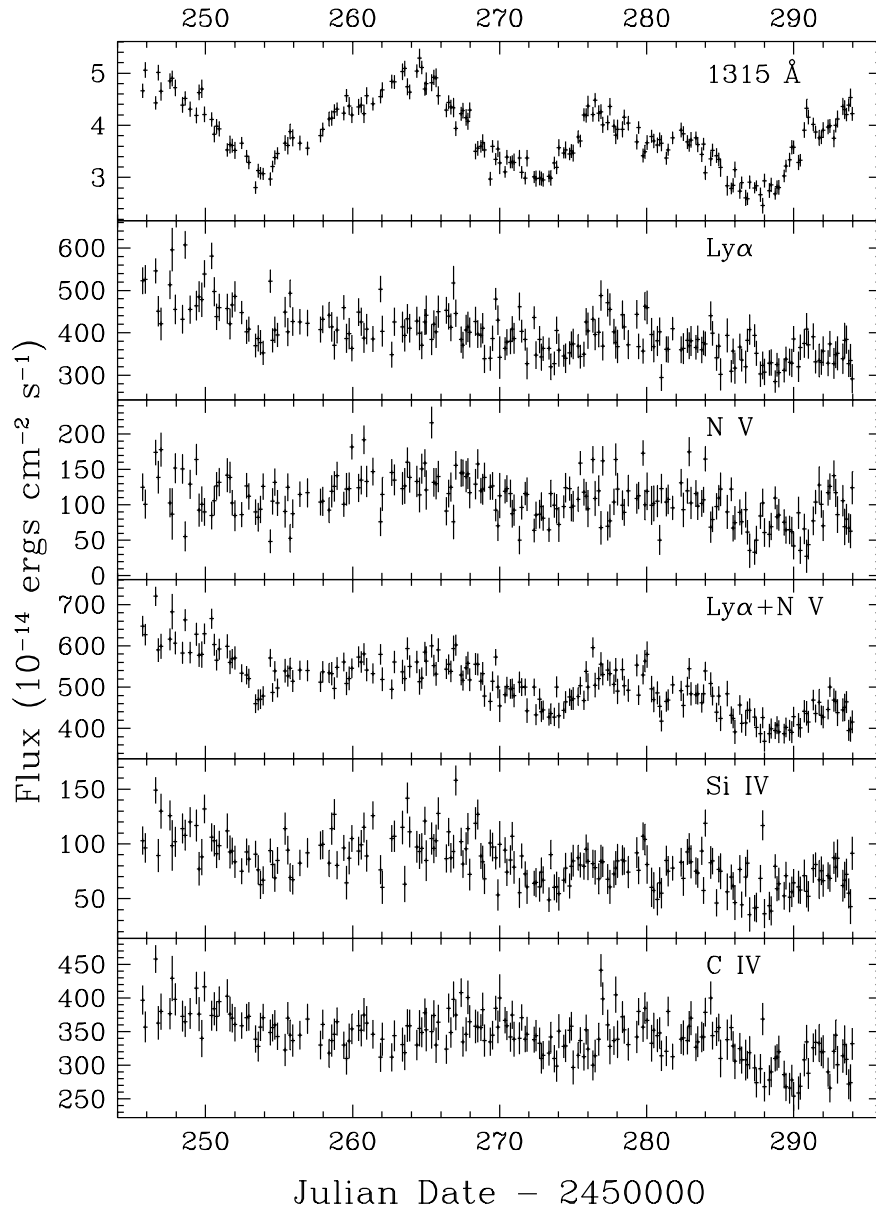
FIG. 8.— Light curves for the strongest emission lines from the 1996 campaign on NGC 7469 extracted from the IUE spectra using the FOS spectrum as a template. For comparison, the top panel gives the F(1315Å) continuum light curve (in units of 10^{-14} ergs cm^{-2} s^{-1} $^{-1}$).

lated values of normalization and spectral index, we generated flux points at 1315 Å, 1485 Å, 1740 Å, and 1825 Å. We used the ICCF technique to measure the time delay for the centroid of the CCF peak in these simulated light curves. For a total of 700 Monte Carlo realizations, relative to the flux at 1315 Å, we find median time delays of 0.09 ± 0.03, 0.026 ± 0.07, and 0.32 ± 0.08 for the fluxes at 1485 Å, 1740 Å, and 1825 Å, respectively, where the error bars represent the 1σ confidence intervals. Thus, from our fits to the IUE data, we can conclude with confidence that the flux at longer wavelengths lags the flux at shorter wavelengths, but we cannot conclude that the lag increases as a function of wavelength. This requires the use of the optical continuum measurements as discussed in §5.1.

4. ASCA OBSERVATIONS OF NGC 7469

Guainazzi et al. (1994) observed NGC 7469 using ASCA between 1993 November 24 and 1993 November 26 for a total exposure time of $\sim$40 ks. Their analysis of these data note the Fe Kα emission feature and a soft excess, but find no evidence for a warm absorber. Subsequent analysis of these same data, benefiting from improved calibration, by Reynolds (1997) and George et al. (1998), however, *do* clearly detect absorption edges of O VII and O VIII indicative of ionized absorbing gas. Reynolds (1997) finds optical depths in the edges of $\tau_{O7} = 0.17$ and $\tau_{O8} = 0.03$.

To examine whether the UV absorption noted in our FOS spectrum of NGC 7469 could be interpreted in the context of a combined X-ray and UV absorber (e.g., Mathur, Wilkes, & Elvis 1995), we have retrieved the ASCA data discussed by Guainazzi et al. from the High Energy Astrophysics Science Archive Research Center. These data have been reprocessed
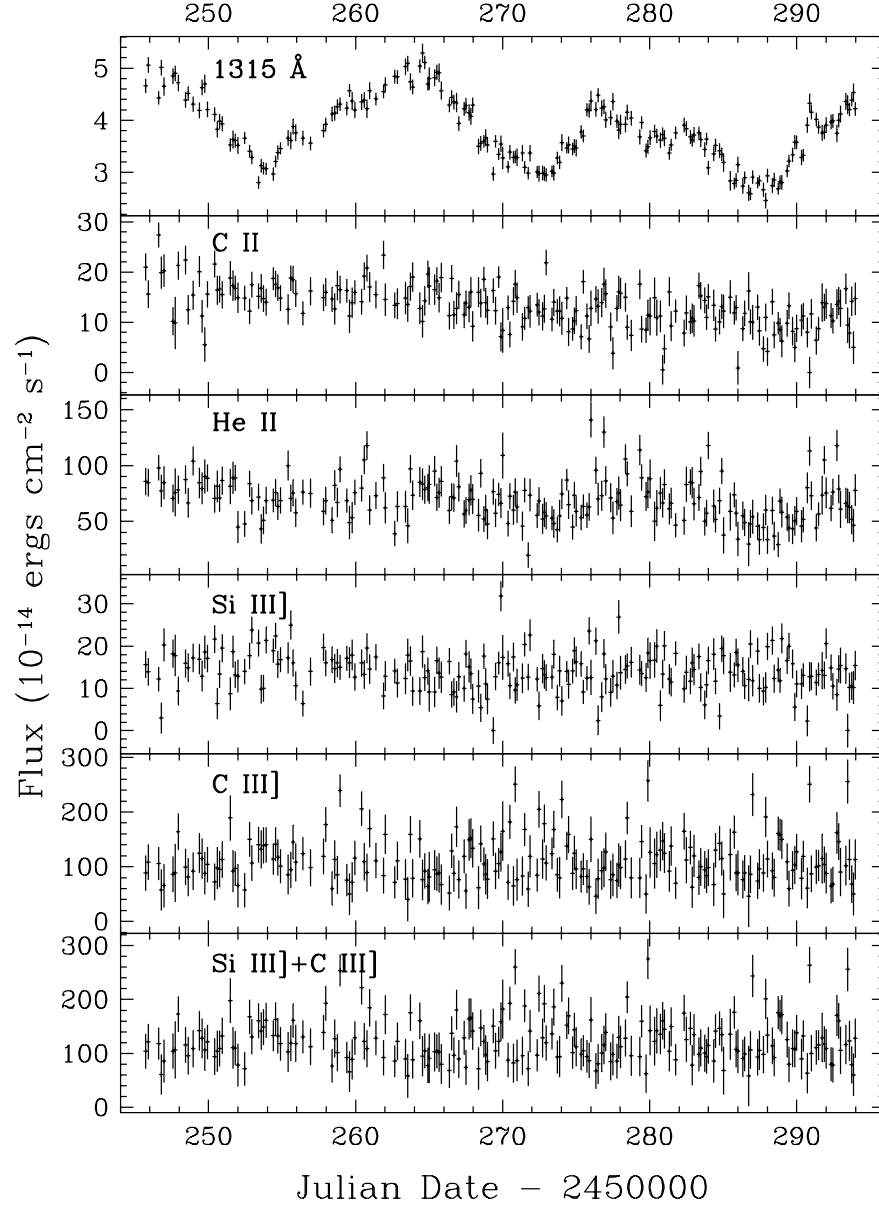
FIG. 9.— Light curves for intermediate-strength emission lines from the 1996 campaign on NGC 7469 extracted from the IUE spectra using the FOS spectrum as a template. For comparison, the top panel gives the F(1315Å) continuum light curve (in units of 10^{-14} ergs cm^{-2} s^{-1} $^{-1}$).

with the "Revision 1" software and calibration, and we have used the screened event files produced by this process. The acceptable SIS data produced by this filtering includes all data obtained outside of the South Atlantic Anomaly, above a limb angle of $10°$ from the dark earth and $20°$ from the bright earth, and in regions of geomagnetic rigidity exceeding 6 GeV c^{-1}. In addition, we eliminated all data intervals with anomalously high count rates; the mean rates were 1.5 cts s^{-1} and 1.1 cts s^{-1} in the SIS0 and SIS1 detectors, respectively, and we excluded data with rates > 3.0 cts s^{-1}. So that Gaussian statistics were applicable in our spectral analysis, we grouped the extracted spectra for the SIS0 and SIS1 detectors so that each energy bin contained a minimum of 25 counts. To avoid the worst uncertainties in the detector response, we restricted our spectral fits described below to bins with energies in the range 0.6 keV < E < 10.0 keV.

Before fitting these data with our warm absorber models, we first verified that our methods produced empirical results compatible with previous analyses. We use v10.0 of the X-ray spectral fitting program XSPEC (Arnaud 1996) for our fits. We note that a simple power law with absorption by cold gas gives an unacceptable fit: $\chi^2 = 661.4$ for 424 data bins and 3 free parameters. Adding a narrow (unresolved) Fe Kα line markedly improves the fit: $\chi^2 = 636.4$ for 424 points and 5 free parameters. A broad Fe Kα line gives further significant improvements, with $\chi^2 = 565.3$ for 424 points and 8 parameters. Our best empirical fit to the data is for a power law continuum, absorption by cold Galactic gas, broad and narrow Fe Kα emission from the source, and two absorption edges representing intrinsic ionized oxygen absorption. This best fit has $\chi^2 = 482.1$ for 424 points and 12 free parameters. The best-fit values for the free parameters are summarized in Table 9.
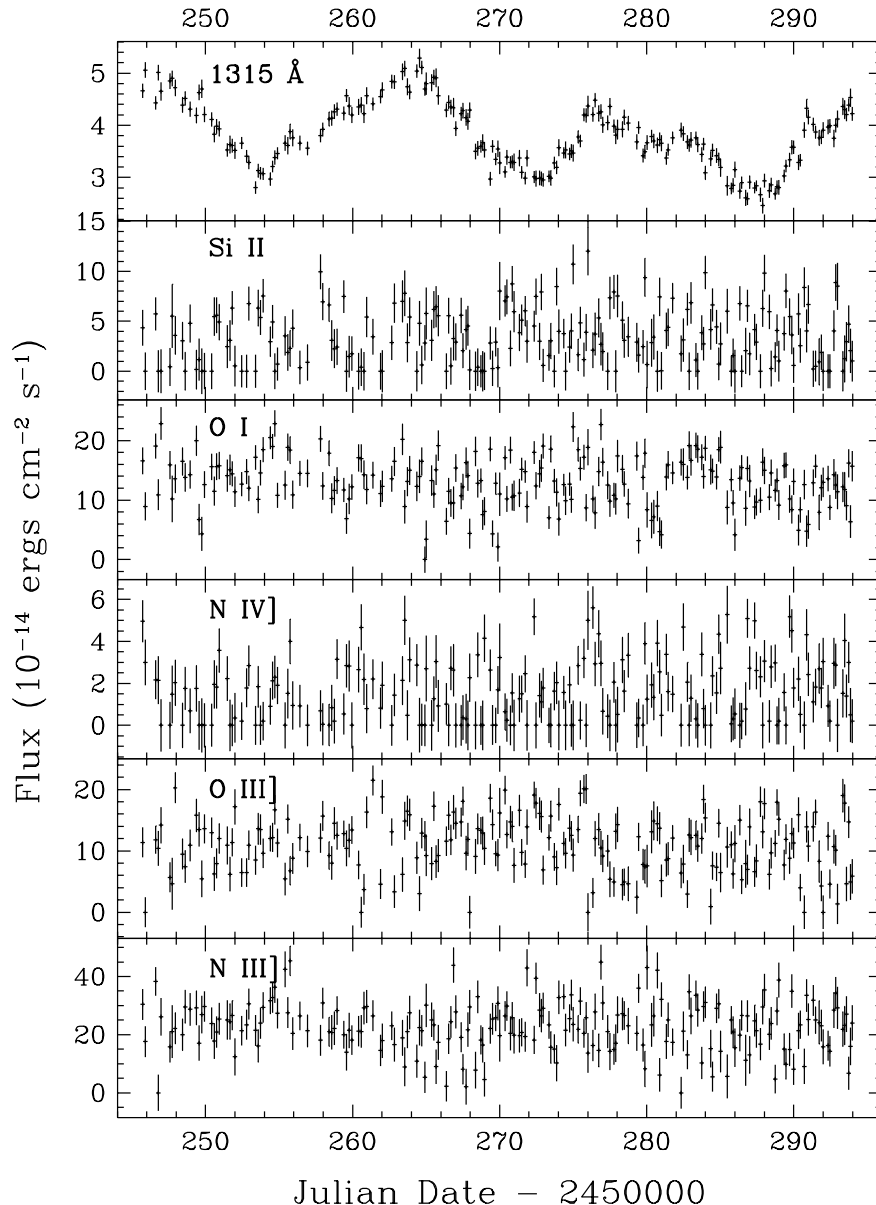
FIG. 10.— Light curves for weak emission lines from the 1996 campaign on NGC 7469 extracted from the IUE spectra using the FOS spectrum as a template. For comparison, the top panel gives the F(1315Å) continuum light curve (in units of 10^{-14} ergs cm^{-2} s^{-1} $^{-1}$).

Our model differs from Reynolds (1997) in that we have omitted any intrinsic cold-gas absorption, added separate narrow and broad Fe Kα emission lines, permitted the edge absorption energies to vary freely, and binned our data differently, but our results are comparable. Our spectral index of 2.14 ± 0.04 agrees well with his value of 2.11, and our edge depth of 0.21 ± 0.03 for O VII is in good agreement with his value of 0.17. Our optical depth for the O VIII edge of 0.13 ± 0.03, however, is larger than Reynold's value of 0.03. The main reason for this difference is that we have let the edge energies vary freely, while Reynold's fixed them at their redshifted vacuum energies.

We now describe photoionization models for the ionized absorbing gas that can be used to evaluate whether the same absorbing medium is responsible for both the X-ray and the UV absorption. These models are constructed in the same way

as those discussed by Krolik & Kriss (1995) and Kriss et al. (1996b). For our ionizing spectrum, we use a spectral shape for NGC 7469 based on the UV and X-ray data discussed here, and the RXTE data presented by Nandra et al. (1998). The fit to the mean of the IUE data has a spectral index (for $F_\nu \propto \nu^{-\alpha}$) of 1.087. The RXTE data has a mean 2–10 keV flux of 3.4×10^{-11} erg cm^{-2} s^{-1}. We re-normalize the ASCA spectrum above (which has $F(2-10) = 3.5 \times 10^{-11}$ erg cm^{-2} s^{-1}) to this value. Since α_{ox} (the effective spectral index between 2500 Å and 2 keV) is 1.34, we note that the UV and X-ray spectra when extrapolated do not meet at any intermediate energy— the ionizing spectrum must steepen between the UV and X-ray bandpasses. Although the lack of simultaneity between the UV and X-ray observations may play some role in this mismatch, this is a common feature of AGN spectra, and composite QSO spectra suggest that the break occurs around the Lyman limit
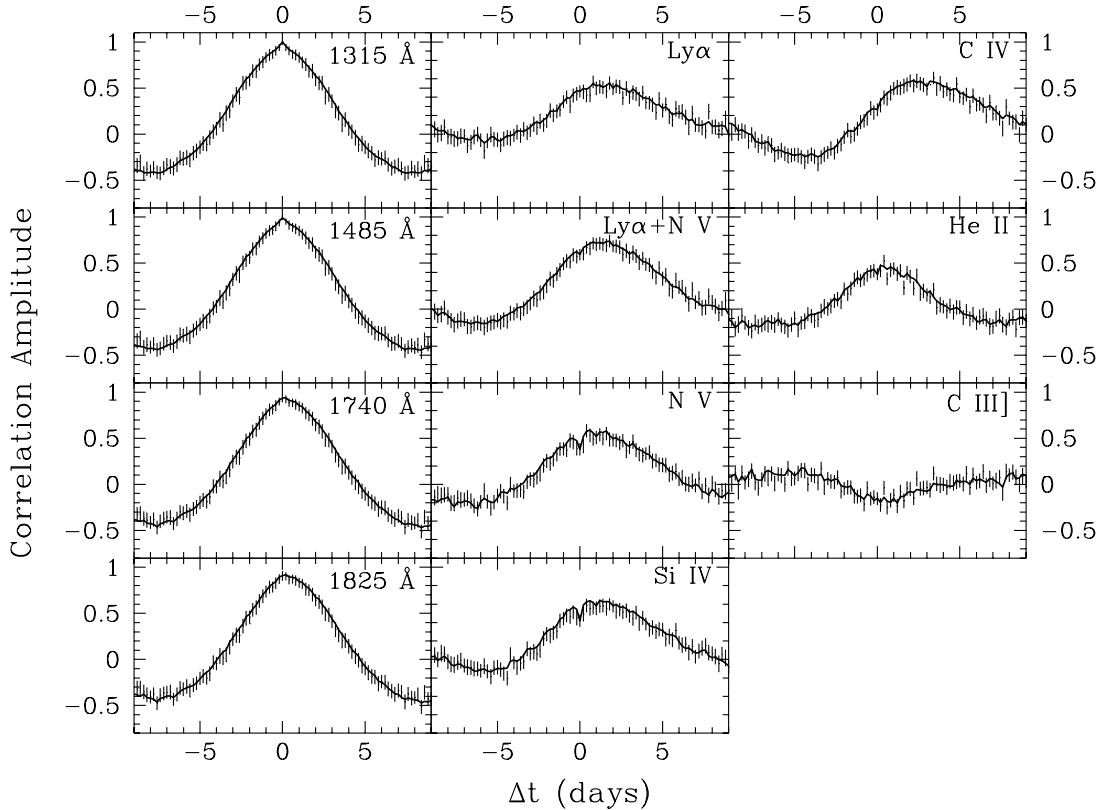
FIG. 11.— The continuum and strong emission-line cross-correlation functions for the fluxes extracted from the IUE spectra of NGC 7469 using the FOS spectrum as a template. Each time series has been cross-correlated with the F(1315Å) flux series. The interpolated version of the cross-correlation function is drawn as a solid line; the error bars are the points from the discrete correlation function.

(Zheng et al. 1997). We therefore extrapolate the UV spectrum to the Lyman limit, and then introduce a spectral break to an index of 1.40 which we follow to an energy of 0.5 keV, where we then flatten to the X-ray energy index of 1.14. Since this spectrum does not diverge to higher energy, we simply extrapolate this to 500 keV for our photoionization calculations.

As in Kriss et al. (1996b), we compute our models in thermal equilibrium, assume constant-density clouds ($n_H = 10^9$ cm^{-3}), and use the ionization parameter $U = n_{ion}/n_H$, where n_{ion} is the number density of ionizing photons between 13.6 eV and 13.6 keV illuminating the cloud and n_H is the density of hydrogen atoms. We assume that the absorbing medium covers 25% of the solid angle around the source. The transmission of each model is computed so that resonant line scattering and electron scattering are fully accounted for (Krolik & Kriss 1995). In computing the widths of the resonance lines, we assume that all ions have turbulent velocities equal to the sound speed in the medium. The transmission is fully described by two parameters, the total column density N_{tot}, and the ionization parameter U.

To fit these models to the ASCA spectra, we assemble our grid of models into a FITS table to be read into XSPEC, and we replace the photoionization edges in our empirical model with the total column density, ionization parameter and redshift of our warm absorber model grid. This gives a result comparable in quality to our best empirical fit: $\chi^2 = 484.2$ for 424 points and 11 free parameters. Best-fit values for the parameters are given in Table 10, and the best-fit spectra are illustrated in Fig. 13.

5. DISCUSSION

5.1. Time Delays and the Case for Continuum Reprocessing

Our newly extracted continuum fluxes for the IUE observations of NGC 7469 in 1996 strengthen the arguments for wavelength-dependent time delays in the continuum flux from this active galaxy. In tests performed on the original data set, Wanders et al. (1997) found that contamination by 10% of a continuum flux interval by a spectral component with a 2-day lag could produce a time delay of ∼0.2 days in the lag measured for the continuum flux. As we note in §3.1, our model of the FOS spectrum indicates that contamination by 15–22% by weak lines and line wings could be present in the continuum fluxes for the bands centered at 1315 Å, 1740 Å and 1825 Å, thus implying that the originally measured lags could be affected by these other spectral features. Our new measurements of the IUE spectra greatly ameliorate the potential level of contamination in the continuum flux points. The new time delays we measure are slightly lower (perhaps reflecting some previous contamination), but the delays are still present, and they increase with increasing wavelength.

As discussed by Collier et al. (1998), a simple model for radiative reprocessing by a steady-state accretion disk with a radial temperature profile determined by viscous heat dissipation predicts that the time delay between different continuum bands should depend on wavelength as $\tau \propto \lambda^{4/3}$, reflecting the $T \propto R^{-3/4}$ temperature profile and the $\tau = R/c$ dependence of the time delay. Fig. 14 shows the measured time delay of the UV and optical continuum points compared to a $\tau \propto \lambda^{4/3}$ curve. Our new measurements are more consistent with this dependence.

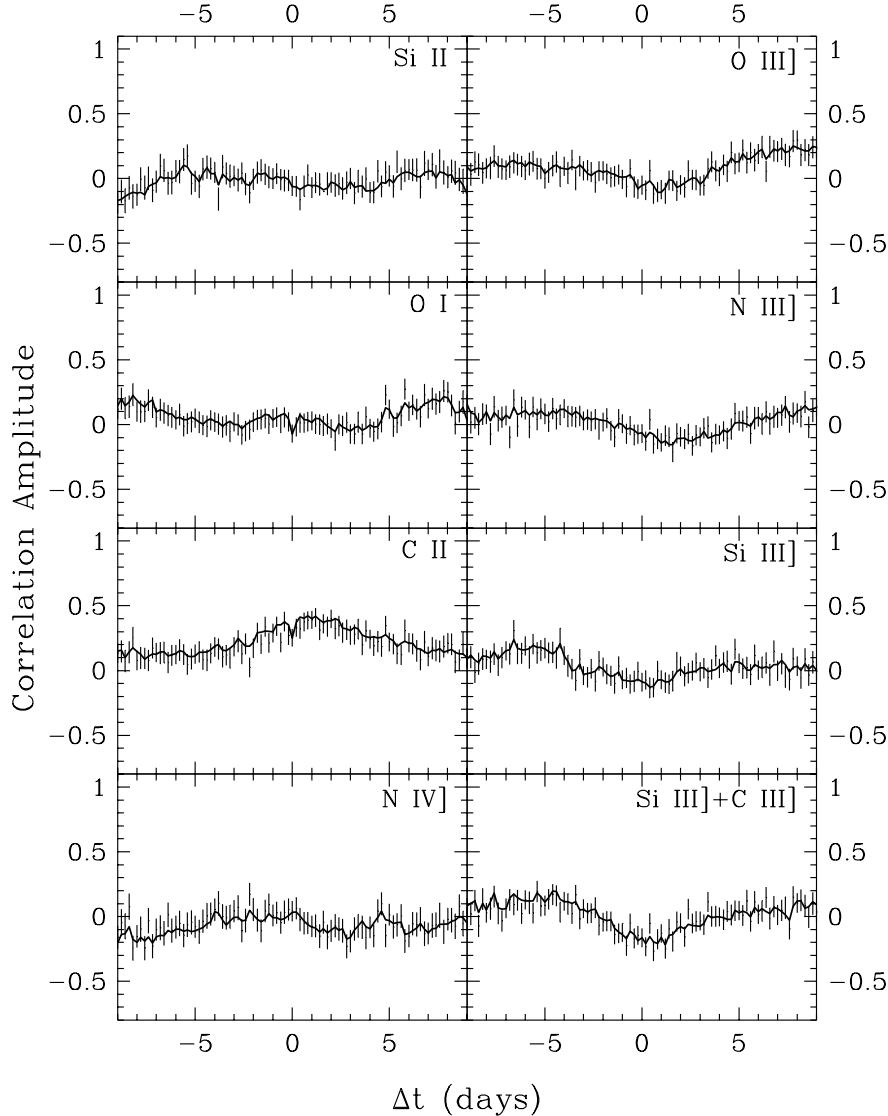While the UV and optical continuum time delays seem in-

FIG. 12.— The weak emission-line cross-correlation functions for the fluxes extracted from the IUE spectra of NGC 7469 using the FOS spectrum as a template. Each time series has been cross-correlated with the F(1315Å) flux series. The interpolated version of the cross-correlation function is drawn as a solid line; the error bars are the points from the discrete correlation function.

dicative of radiative reprocessing, the puzzle remains— what radiation is being reprocessed? As Nandra et al. (1998) show, producing the UV and optical continuum in NGC 7469 via reprocessing of the X-ray radiation is not energetically feasible, nor does it have the requisite time dependence. Simultaneous EUVE, ASCA, and RXTE observations of NGC 5548 by Chiang et al. (1999) show that the X-ray variations lag the EUV variations, and that therefore the EUV cannot be produced via reprocessing of the hard X-rays.

Nandra et al.'s detailed comparison of the X-ray and UV continuum light curves in the NGC 7469 campaign shows fairly complex behavior. The main positive correlation is a 4-day lag in which the UV leads the X-ray continuum. This is largely due to the peaks in the UV light curve leading the X-ray peaks. In contrast, the light-curve minima are nearly simultaneous. Nandra et al. (1998) suggest that the longer timescale X-ray variability is due to upscattering of UV seed photons from a variety of sources at different distances that leads to multiple lags. At high flux levels, the source of the UV seed photons lies at a distance of ~ 4 lt days. In the flux minima, the seed photons arise

closer to the X-ray production region. The most rapid X-ray variations are due to variations in the particle distribution of the scattering medium. In addition, they suggest that some portion of the EUV continuum is produced by X-ray reprocessing, and that this is what drives the line radiation.

Such a scenario poses severe problems for the relative geometry of the continuum production zone and the broad-line cloud region (BLR), however. It also is at odds with simultaneous EUVE, ASCA, and RXTE observations of NGC 5548 (Chiang et al. 1999) that show that X-ray variations lag the EUV variations, and that therefore the EUV cannot be produced via reprocessing of the hard X-rays. In NGC 7469, all the broad lines have measured lags < 4 lt days. If the X-ray radiation is produced closest to the black hole, the scenario proposed by Nandra et al. would imply that the EUV production zone and the BLR lie between the X-ray and UV production zones. Another problem is then one of scale— 4 lt days from a $10^7 M_\odot$ black hole corresponds to 7000 gravitational radii (GM/c^2). This is a factor of more than 100 higher than the radius at which viscous dissipation in an accretion disk produces UV and optical

continuum radiation. Producing the majority of UV and optical radiation at such large radii requires a new, highly efficient dissipation mechanism.

TABLE 8
CROSS-CORRELATION RESULTS

Feature	τ_{cent} (days)	τ_{peak} (days)	r_{max}	FWHM (days)
$F_\lambda(1315$ Å$)$	$0.00^{+0.09}_{-0.09}$	$0.00^{+0.05}_{-0.04}$	1.00	5.11
$F_\lambda(1485$ Å$)$	$0.09^{+0.11}_{-0.08}$	$0.02^{+0.04}_{-0.06}$	0.99	5.12
$F_\lambda(1740$ Å$)$	$0.28^{+0.12}_{-0.13}$	$0.06^{+0.14}_{-0.02}$	0.95	5.10
$F_\lambda(1825$ Å$)$	$0.36^{+0.11}_{-0.17}$	$0.08^{+0.20}_{-0.02}$	0.93	5.12
$F_\lambda(4945$ Å$)$	$1.17^{+0.55}_{-0.33}$	$1.33^{+0.35}_{-0.58}$	0.89	5.60
$F_\lambda(6962$ Å$)$	$1.68^{+1.12}_{-0.82}$	$1.43^{+1.67}_{-0.53}$	0.71	6.09
Lyα	$1.30^{+0.61}_{-0.50}$	$1.76^{+0.39}_{-1.06}$	0.56	6.61
Lyα+N v	$1.48^{+0.28}_{-0.38}$	$1.71^{+0.04}_{-0.96}$	0.74	6.37
N v	$1.24^{+0.41}_{-0.63}$	$0.58^{+1.07}_{-0.13}$	0.59	5.99
Si iv	$1.50^{+0.37}_{-0.71}$	$1.24^{+0.56}_{-0.79}$	0.65	6.30
C iv	$2.81^{+0.62}_{-0.87}$	$2.24^{+1.26}_{-0.39}$	0.59	6.38
He ii	$0.67^{+0.27}_{-0.64}$	$0.31^{+0.64}_{-0.51}$	0.48	4.38
C iii]	—	—	0.18	—
Si ii]	—	—	0.13	—
O i]	—	—	0.23	—
C ii	$1.33^{+0.93}_{-1.86}$	$1.06^{+1.29}_{-1.56}$	0.42	7.27
N iv]	—	—	0.14	—
O iii]	—	—	0.25	—
N iii]	—	—	0.19	—
Si iii]	—	—	0.24	—
Si iii]+C iii]	—	—	0.20	—

TABLE 9
EMPIRICAL FIT TO NGC 7469 X-RAY SPECTRUM

Parameter	Best-fit Value
Photon index, α	2.14 ± 0.04
Power law normalization, F_{1keV}	$(1.36 \pm 0.04) \times 10^{-2}$ phot cm^{-2} s^{-1} keV^{-1}
N_{HI}	$(4.4 \pm 1.0) \times 10^{20}$ cm^{-2}
Edge Energy, E_{O7}[a]	0.685 ± 0.021 keV
Optical Depth, τ_{O7}	0.21 ± 0.04
Edge Energy, E_{O8}[a]	0.848 ± 0.021 keV
Optical Depth, τ_{O8}	0.13 ± 0.03
Narrow Fe Energy[a]	6.345 ± 0.031 keV
Narrow Fe EW	47 ± 18 eV
Narrow Fe width, σ	Fixed at 0.0
Broad Fe Energy[a]	7.03 ± 0.29 keV
Broad Fe EW	3.14 ± 0.82 keV
Broad Fe width, σ	2.24 ± 0.48 keV
χ^2/dof	482.11/412

[a]Energy in the rest frame of NGC 7469, $z = 0.0164$.

5.2. *UV and X-ray Absorption in NGC 7469*

The far-UV spectrum of NGC 7469 as seen with the FOS is typical of other Seyfert 1s and low redshift AGN. The intrinsic absorption lines, while hinted at in earlier IUE spectra, show up clearly. Like most other Seyfert 1s in which these features are seen, the equivalent widths (EWs) of 1 Å or less are difficult to detect in the lower resolution, lower S/N IUE spectra. With the FOS (and the GHRS), they are now seen to be a common feature of Seyfert 1s (Crenshaw et al. 1999), as common as the "warm absorbers" seen in ROSAT and ASCA X-ray spectra (e.g., Turner et al. 1993; Mathur et al. 1994; Nandra & Pounds 1994; Fabian et al. 1994; Reynolds 1997; George et al. 1998).

Mathur et al. (1994, 1995) have suggested a link between the two phenomena, in which the UV absorption lines are produced by the minority ions in the photoionized gas which is producing the X-ray absorption.
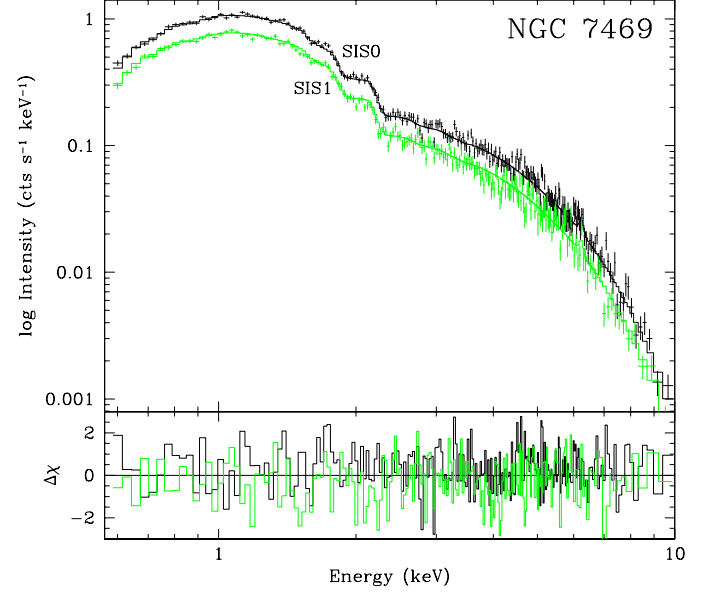

FIG. 13.— *Upper Panel:* The solid lines are the best-fit warm absorber model for NGC 7469 folded through the ASCA SIS0 and SIS1 detector responses. The data points are crosses with 1σ error bars. The model includes a power law with photon index 2.25, absorption by neutral gas with an equivalent neutral hydrogen column of $N_H = 5.8 \times 10^{20}$ cm^{-2}, absorption by ionized gas with a total column density log $N_{tot} = 21.6$ cm^{-2} and an ionization parameter of $U = 2.0$, an unresolved iron Kα line at 6.24 keV with an equivalent width of 46 eV, and a broad (FWHM = 5.9 keV) iron Kα line at 6.78 keV with an equivalent width of 4 keV. *Lower Panel:* The contributions to χ^2 of each spectral bin are shown. The solid line is for SIS0 and the dotted line for SIS1.

To test whether this is consistent with the strength of the UV absorption lines seen in NGC 7469, we can calculate the column densities of the UV ion species using our warm absorber model fit to the X-ray spectrum. If this single-zone model can simultaneously account for both the X-ray and the UV absorbers, then the observed EWs of the UV lines should fall on a single curve of growth consistent with the model. In Fig. 15 we plot the observed EWs of the Lyα, N v, and C iv absorption lines at the column densities predicted by the best-fit X-ray warm absorber model. One can see that this is not a self-consistent description of both the X-ray and UV-absorbing gas. In particular, the strength of the C iv absorption lines is much higher than would be predicted for the residual column in gas ionized sufficiently to produce the observed X-ray absorption.

The observed UV absorption is more consistent with lower column density gas at a lower ionization parameter. Fig. 16 shows curves of growth for a photoionization model that provides the best match to the observed UV absorption lines. With a total column density of log $N_{tot} = 19.2$ cm^{-2} and an ionization parameter of $U = 0.04$, the observed EWs of Lyα, N v, and C iv are nearly all consistent with gas having a Doppler parameter of ~ 25 km s^{-1}. The total column of this UV-absorbing component is low enough that it would have negligible effect on the appearance of the X-ray spectrum. Similarly, as shown by a comparison of Figures 15 and 16, the X-ray absorbing gas makes little contribution to the UV absorption lines.

TABLE 10
WARM ABSORBER FIT TO NGC 7469 X-RAY SPECTRUM

Parameter	Best-fit Value
Photon index, α	2.25 ± 0.06
Power law normalization, F_{1keV}	$(1.56 \pm 0.08) \times 10^{-2}$ phot cm^{-2} s^{-1} keV^{-1}
N_H	$(5.8 \pm 1.2) \times 10^{20}$ cm^{-2}
Total Column Density, log N_{tot}	21.6 ± 0.08 cm^{-2}
Ionization Parameter, U	2.0 ± 0.4
Redshift, z	0.058 ± 0.0012
Narrow Fe Energy	6.239 ± 0.036 keV
Narrow Fe EW	46 ± 34 eV
Narrow Fe width, σ	Fixed at 0.0
Broad Fe Energy	6.78 ± 0.33 keV
Broad Fe EW	4.1 ± 1.2 keV
Broad Fe width, σ	2.5 ± 0.6 keV
χ^2/dof	484.20/413
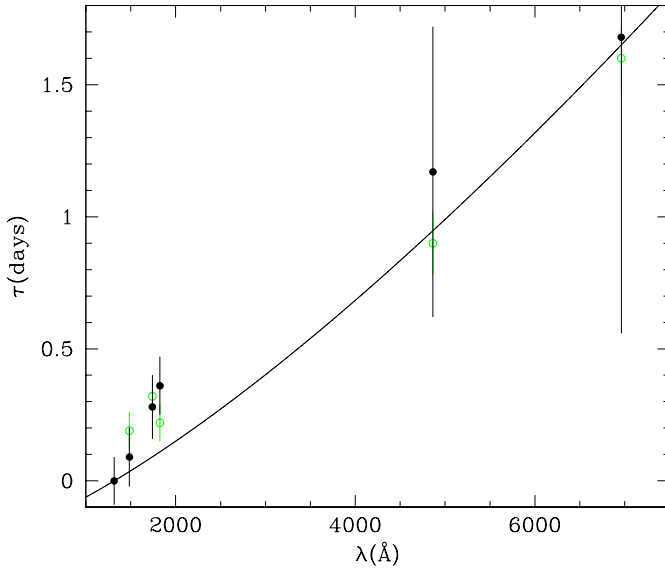
FIG. 14.— Time delays vs. wavelength for the IUE continuum bands and the optical bands presented by Collier et al. (1998). The gray open circles represent the original measurements of the IUE data from Wanders et al. (1997) and the optical data from Collier et al. (1998). The filled black circles are the new measurements from this paper. The solid line shows the $\lambda^{4/3}$ dependence via the function $\tau = 3.0((\lambda/10^4)^{4/3} - (1315/10^4)^{4/3})$.

Thus NGC 7469 is yet another instance of a Seyfert galaxy possessing a complex assortment of absorbing regions. This was previously shown to be true for NGC 4151 (Kriss et al. 1995) and for NGC 3516 (Kriss et al. 1996a). The case of NGC 3516 is particularly illuminating since high resolution UV spectra show that multiple kinematic components are present, an additional indication that multiple regions are contributing to the absorption (Crenshaw, Maran, & Mushotzky 1998). The Seyferts NGC 4151 (Weymann et al. 1997) and NGC 5548 (Crenshaw et al. 1999; Mathur, Elvis, & Wilkes 1999) also appear kinematically complex when observed at high spectral resolution. In fact, in NGC 5548, the prototypical example of a combined "XUV" absorber (Mathur, Wilkes, & Elvis 1995), Mathur et al. (1999) now acknowledge that at most one of the six different kinematic components visible in the high-

resolution UV spectrum actually arises in the X-ray absorbing zone. Crenshaw and Kraemer (1999) have identified the kinematic component with the highest blueshift as the one associated with the X-ray absorber in NGC 5548.
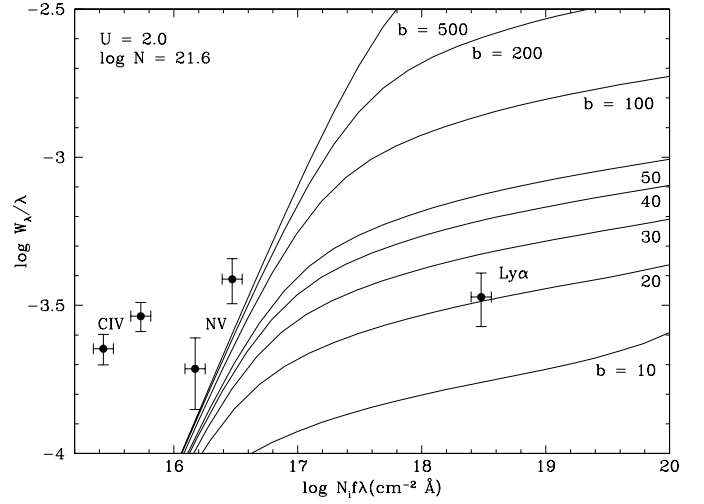

FIG. 15.— The observed EWs of the UV absorption lines in NGC 7469 are plotted on curves of growth using column densities predicted by the single warm absorber fit to the ASCA X-ray spectrum. This model has $U = 2.0$ and a total column density of log $N_{tot} = 21.6$ cm^{-2}. Points are plotted at a horizontal position determined by the column density for the given ion in the model with a vertical coordinate determined by the observed EW for the corresponding absorption line. The vertical error bars are from Table 2, and the horizontal error bars are the range in column density allowed by the uncertainty in the fit to the ASCA spectrum. The thin solid lines show predicted EWs as a function of column density for Voigt profiles with Doppler parameters of $b = 10, 20, 30, 40, 50, 100, 200,$ and 500 km s^{-1}. A model that fits the data would have all points lying on one of these curves. This model cannot simultaneously match both the UV and the X-ray absorption.
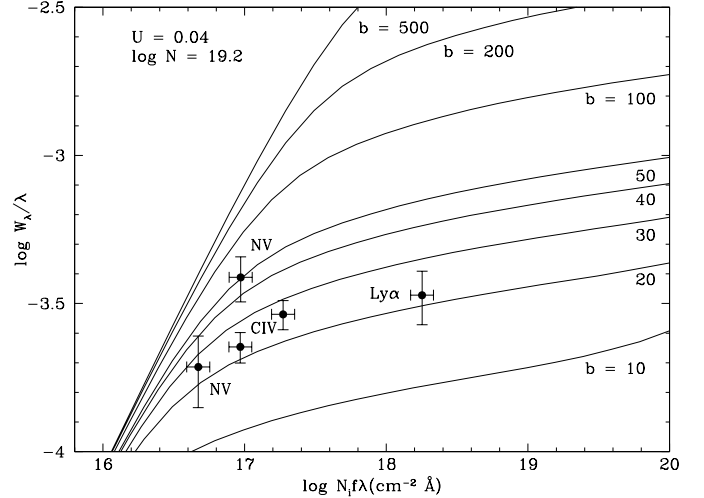

FIG. 16.— As in Fig. 15, but for a photoionization model with $U = 0.04$ and log $N_{tot} = 19.2$ cm^{-2}. A curve of growth with $b \sim 25$ km s^{-1} can match nearly all the observed EWs.

While most Seyferts with UV and X-ray absorption appear to have a complex assortment of absorbing regions with a broad range of physical conditions, this does not mean that these

physically distinct regions are unrelated. Since UV and X-ray absorption (or the lack of both) appears to be linked in most Seyferts (Crenshaw et al. 1999), it is likely that a common mechanism is responsible for both. Possibilities for this mechanism include outflows of material ablated from the obscuring torus (Weymann et al. 1991; Kriss et al. 1995), or a wind from the accretion disk (Königl & Kartje 1994; Murray et al. 1995). A natural origin for the separate UV and X-ray absorbing clouds would be to have higher density clumps embedded in a more tenuous wind. The smaller, higher density clumps would have lower total column densities and lower ionization parameters, a requirement for the UV absorbers. The tenuous surrounding wind (which may well have a range of physical conditions itself, e.g. Kriss et al. 1996b) could be the source for the X-ray warm absorber. In such a scenario one might also expect to see correlated variability in the total column density of the X-ray and UV absorbers related to "events" in which new material was ablated from the torus or accretion disk into the outflowing wind.

6. SUMMARY

We have used a high S/N FOS spectrum of NGC 7469 to produce a model template for extracting deblended emission line and continuum fluxes from the series of IUE spectra obtained in the 1996 monitoring campaign. The FOS spectrum shows that "continuum" windows at 1315 Å, 1740 Å and 1825 Å used by Wanders et al. (1997) in the original analysis have significant contaminating contributions from the wings of the broad emission lines and other low-level features such as O I λ1304 and Fe II emission lines. Our new extractions for the most part eliminate these contaminating components from the measured fluxes. Using these cleaner data, we still find a time delay in the the response of the continuum flux at longer wavelengths relative to shorter wavelengths. We find time delays of 0.09,

0.28, and 0.36 days for the fluxes at 1485 Å, 1740 Å and 1825 Å, respectively, relative to F(1315 Å). When combined with the delays measured for the optical continuum by Collier et al. (1998), we find that the wavelength dependence of the time-delay follows a $\lambda^{4/3}$ relation that is consistent with the simplest models of radiative reprocessing.

The FOS spectrum of NGC 7469 reveals associated absorption in the high-ionization lines N V, C IV and Lyα, a common feature of Seyfert galaxies (Crenshaw et al. 1999). The X-ray spectrum of NGC 7469 also shows evidence for an ionized absorber (Reynolds 1997; George et al. 1998), and we have analyzed the UV and X-ray absorbers in the context of a single UV/X-ray absorber (Mathur, Wilkes, & Elvis 1995). We find, however, that such a unified description is untenable. The predicted column densities of UV-absorbing ions in the best-fitting warm absorber model for the X-ray spectrum imply line strengths well below those observed. The UV absorption requires gas with a lower ionization parameter and lower column density. Even though the X-ray and UV absorption in this Seyfert and in many others requires a complex assortment of kinematic components with different physical conditions, the fact that associated UV absorption and X-ray warm absorbers are often found in the same objects (Crenshaw et al. 1999) suggests that the material for each of these absorbers has a common origin.

REFERENCES

Arnaud, K. A., 1996, in "Astronomical Data Analysis Software and Systems V", ASP Conf. Series 101, eds. G. Jacoby & J. Barnes, (San Francisco: ASP), 17
Avni, Y. 1976, ApJ, 210, 642
Blandford, R.D., & McKee, C.F. 1982, ApJ, 255, 419
Cardelli, J., Clayton, G., & Mathis, J. 1989, ApJ, 345, 245
Chiang, J., et al., ApJ, in press
Clavel, J., et al. 1991, ApJ, 366, 64
Collier, S., et al. 1998, ApJ, 500, 162
Crenshaw. D. M., & Kraemer, S. B., 1999, ApJ, in press
Crenshaw. D. M., Kraemer, S. B., Boggess, A., Maran, S. P., Mushotzky, R. F., & Wu, C. C. 1999, ApJ, 516, 750
Crenshaw. D. M., Maran, S. P., & Mushotzky, R. F. 1998, ApJ, 496, 797
Edelson, R. A., & Krolik, J. H. 1988, ApJ, 333, 646
Elvis, M., Lockman, F. J., & Wilkes, B. J. 1989, AJ, 97, 777
Fabian, A. C., et al. 1994, PASJ, 46, L59
Gaskell, C. M., & Peterson, B. M. 1987, ApJS, 65, 1
Gaskell, C. M., & Sparke, L. S. 1986, ApJ, 305, 175
George, I. M., Turner, T. J., Netzer, H., Nandra, K., Mushotzky, R. F., & Yaqoob, T. 1998, ApJS, 114, 73
Guainazzi, M., Matsuoka, M., Piro, L., Mihara, T., & Yamauchi, M. 1994, ApJ, 436, L35
Horne, K., Welsh, W.F., & Peterson, B.M. 1991, ApJL, 367, L5
Königl, A., & Kartje, J. F. 1994, ApJ, 434, 446
Korista, K. T., et al. 1995, ApJS, 97, 285
Kriss, G. A. 1994a, in Astronomical Data Analysis Software and Systems III, ASP Conf. Ser. 61, ed. D. R. Crabtree, R. J. Hanisch, & J. Barnes, (San Francisco: ASP), 437
Kriss, G. A., Davidsen, A. F., Zheng, W., Kruk, J. W., & Espey, B. R. 1995, ApJ, 454, L7
Kriss G. A., et al. 1996a, ApJ, 467, 622
Kriss G. A., et al. 1996b, ApJ, 467, 629

Krolik, J. H., & Kriss, G. A. 1995, ApJ, 447, 512
Krolik, J. H., et al. 1991, ApJ, 371, 541
Mathur, S., Elvis, M., & Wilkes, B. 1999, ApJ, 519, 605
Mathur, S., Wilkes, B., & Elvis, M. 1995, ApJ, 452, 230
Mathur, S., Wilkes, B., Elvis, M., & Fiore, F. 1994, ApJ, 434, 493
Murray, N., Chiang, J., Grossman, S. A., Voigt, G. M. 1995, ApJ, 451, 498
Nandra, K., & Pounds, K. 1994, MNRAS, 268, 405
Nandra, K., et al., 1998, ApJ, 505, 594
Osterbrock, D. E. 1963, Planet. Space Sci., 11, 621
Peterson, B.M. 1993, PASP, 105, 247
Peterson, B.M., Wanders, I., Horne, K., Collier, S., Alexander, T., Kaspi, S., & Maoz, D. 1998, PASP, 110, 660
Reichert, G. A., et al. 1994, ApJ, 425, 582
Reynolds, C. S. 1997, MNRAS, 286, 513
Rodríguez-Pascual, P.M., et al. 1997, ApJS, 110, 9
Shull, J. M., & Van Steenberg, M. E. 1985, ApJ, 294, 599
Telfer, R. C., Kriss, G. A., Zheng, W., Davidsen, A. F., & Green, R. F. 1998, ApJ, 509, 132
Turner, T.J., Nandra, K., George, I.M., Fabian, A.C., & Pounds, K.A. 1993, ApJ, 419, 127
de Vaucouleurs, G., de Vaucouleurs, A., Corwin, H. G., Buta, R. J., Paturel, G., & Fouqué, P. 1991, Third Reference Catalogue of Bright Galaxies (Springer, New York)
Wanders, I., et al. 1997, ApJS, 113, 69
Welsh, W.F., Peterson, B.M., Koratkar, A.P., & Korista, K.T. 1998, ApJ, 509, 118
Weymann, R. J., Morris, S. L., Foltz, C. B., & Hewett, P. C. 1991, ApJ, 373, 23
Weymann, R. J., Morris, S. L., Gray, M. L., & Hutchings, J. B. 1997, ApJ, 483, 717
White, R. J., & Peterson, B. M. 1994, PASP, 106, 879
Zheng, W., Kriss, G. A., Telfer, R. C., Grimes, J. P. & Davidsen, A. F. 1997, ApJ, 475, 469